Microtubule anchoring and coupling of CD20 to the RhoA/Rock1 pathway

Kathrin Kläsener[1,2,3,a,✉], Cindy Eunhee Lee[4,9,a], Julian Bender[5], Angela Naumann[2,6], Lena Reimann[1,7], Geoffroy Andrieux[8], Nadja Herrmann[2], Roland Nitschke[2,6], Klaus Warnatz[3,9], Bettina Warscheid[5], Reinhard E. Voll[3], Michael Reth[1,2,3,✉]

[1] Biology III, Faculty of Biology, University of Freiburg, Freiburg, Germany
[2] Signaling Research Centers BIOSS and CIBSS, University of Freiburg, Freiburg, Germany
[3] Department of Rheumatology and Clinical Immunology, Medical Center –Faculty of Medicine, University of Freiburg, Freiburg, Germany
[4] Faculty of Science and Technology, University of Canberra, Canberra, Australia
[5] Biochemistry II, Theodor-Boveri-Institute, Biocenter, Faculty of Chemistry and Pharmacy, University of Würzburg, Würzburg, Germany
[6] Life Imaging Center and Signalling Research Centres CIBSS and BIOSS, University of Freiburg, Freiburg, Germany.
[7] Celonic AG, Basel, Switzerland
[8] Institute of Medical Bioinformatics and Systems Medicine, Medical Center - Faculty of Medicine, University of Freiburg, Freiburg, Germany
[9] Center for Chronic Immunodeficiency (CCI), Medical center - Faculty of medicine, University of Freiburg, Freiburg, Germany
[a] equal contributors

*** Correspondence:**

✉Dr. Michael Reth. Department of Rheumatology and Clinical Immunology, Medical Center University of Freiburg, Germany and BIOSS, Signalhaus Freiburg, Schänzlestr.18 D-79104 Freiburg, Tel.: +49 761 2032718, E-mail: michael.reth@bioss.uni-freiburg.de

✉Dr. Kathrin Kläsener. Department of Rheumatology and Clinical Immunology, Medical Center University of Freiburg, Germany and BIOSS, Signalhaus Freiburg, Schänzlestr.18 D-79104 Freiburg, Tel.: +49 761 2032730, E-mail: kathrin.klaesener@bioss.uni-freiburg.de

Abstract

CD20 is a B cell-specific four-helix transmembrane protein and a prominent target of therapeutic anti-CD20 antibodies. We have recently described that CD20 is localized within a membrane nanocluster harboring the IgD class B cell antigen receptor (IgD-BCR) where it functions as a gatekeeper for the resting state of naïve human B lymphocytes. How CD20 exerts its gatekeeper function is not yet known. Using Ramos and human peripheral blood B cells, we show here that the serine/threonine kinase PKCδ, constitutively phosphorylates serine residues at the cytosolic tails of CD20. The phosphorylated CD20 becomes a target for 14-3-3 adaptor proteins that link CD20 to the RhoA GDP/GTP exchange factor GEF-H1 and the microtubule (MT) network controlling the stability of the IgD-BCR nanocluster. Binding of anti-CD20 antibodies results in MT disassembly and the replacement of the GEF-H1/CD20 complex by a RhoA-GTP/ROCK1/CD20 complex which drives actomyosin contractility. Our study suggests that CD20 not only maintains the resting state, but also orchestrates the MT/actin switch in active B lymphocytes. This could have implications for treatment with anti-CD20 antibodies and may help to optimize therapeutic protocols.

Keywords: anti-CD20 therapeutic antibody / B lymphocyte / MT network / PKCδ / RhoA-Rock1 pathway.

Introduction

Upon a successful production of an immunoglobulin heavy and light chain pair, pre-B cells become immature B cells expressing an IgM-class B cell antigen receptor (IgM-BCR). The IgM-BCR plays an important role for the central tolerance process where immature B cells undergo negative selection to eliminate self-reactive clones. After surviving selection, immature B cells further develop into transitional B cells that migrate to secondary lymphoid organs and then into mature naive B cells co-expressing an IgM and IgD-BCR[1]. According to the clonal selection theory, mature B cells only become fully activated upon binding to their cognate antigen. Thus, most mature naive B cells remain in a dormant state and the IgD-BCR plays an important role for the maintenance of this resting state. We have previously shown that the IgM-BCR and IgD-BCR are localized in different membrane nanoclusters[2]. The IgD-BCR nanocluster has a raft-type lipid composition and harbors important B cell coreceptors such as CD19, CD20, CD40 and the BAFF receptor[3–6]. Interestingly, most proteins residing within the IgD nanocluster including the IgD-BCR reach their full expression level only at the mature naive B cell stage. This is also the case for CD20, a 37 kD non-glycosylated phosphoprotein with four transmembrane domains that form dimers or higher oligomers on the B cell surface[7–9]. The CD20 protein is encoded by the MS4A1 gene and a member of the MS4A gene family. Due to the lack of a known ligand the biological function of CD20 has been regarded as an enigma of B cell biology[10,11]. However, newer data show that CD20 is a highly interactive protein that helps in the regulation and functional organization of other receptors on the B cell surface[12]. For example, CD70 has recently been shown to require the presence of CD20 for immune synapse formation and efficient T: B collaboration[13].

CD20 is best known as a prominent target of therapeutic monoclonal antibodies (mAb) such as rituximab (RTX), obinutuzumab (GA101), or ocrelizumab used for the treatment of B cell chronic lymphocytic leukemia (B-CLL), malignant B cell lymphomas or human autoimmune diseases such as rheumatoid arthritis (RA), systemic lupus erythematosus (SLE) and, more recently, multiple sclerosis (MS)[14–18]. The anti-CD20 mAbs are thought to eliminate targeted B cells by antibody-dependent cellular cytotoxicity (ADCC) mechanisms, phagocytosis[19], or induction of cell cycle arrest and initiation of an apoptosis program in some B cell lines[20]. The success of the anti-CD20 immunotherapy could be further improved by a more profound insight into the biological function of CD20. An important advance for this goal is the finding that CD20 is part of the IgD-BCR nanocluster where it functions as a gatekeeper for the resting state of naïve human B lymphocytes[21]. Here, we show that constitutively phosphorylated serine residues in the N- and C-terminal cytosolic tails of CD20 play an important role for this

gatekeeper function by coupling CD20 to the microtubule (MT) network and the RhoA/ROCK1 signaling pathway.

Results

CD20 is a substrate of PKCδ acting as a gatekeeper for the resting state of B cells

The resting state of naïve human B lymphocytes is maintained by several negative regulators including PKCdelta (PKCδ), a member of the novel serine/threonine protein kinase C (PKC) family[22,23]. PKCδ has been found to be constitutively associated with the BCR signaling subunit Igα (CD79a) and negatively regulates the BCR signaling[24]. To study the gatekeeper function of PKCδ we employed the CRISPR/Cas9 method to generate two PKCδ-deficient (PKCδ KO) clones of the human Burkitt lymphoma cell line Ramos (Fig. S1A and B). The PKCδ KO Ramos cells were viable and could be maintained in culture. We first compared the expression of B cell marker proteins on the surface of the PKCδ KO line to the wild-type (wt) Ramos cells by flow cytometric analysis (Fig. 1A). Normalization of the protein expression levels on PKCδ KO to Ramos wt cells shows that the loss of PKCδ is associated with a 25-fold increase of the B cell activation marker CD69 on Ramos B cells. The PKCδ deficiency also results in the upregulation of membrane proteins that are associated with the IgD-class nanocluster on resting B cells, namely CD20, CD19, CD40 and the IgD-BCR, whereas proteins that are associated with the IgM-BCR, such as CD45 are downregulated. In addition, two membrane proteins that function as negative B cell signaling regulators, namely CD22 and the IgG-binding Fc receptor FcγRIIb are upregulated in the PKCδ KO Ramos line (Fig. 1A). The 20-fold upregulation of the inhibitory FcγRIIb (CD32b) is interesting because mutations of CD32b are associated with human autoimmune diseases such as systemic lupus erythematosus (SLE)[25]. In summary, this study shows that PKCδ KO Ramos B cells are activated and counteract this activation by upregulating the IgD-class nanocluster and negative signaling regulators. These findings support the notion that, similar to CD20, PKCδ acts as a gatekeeper for the “resting state” of mature human B cells[22].

Next, we conducted a phosphoproteome analysis to monitor the difference in the level of constitutive serine/threonine phosphorylation in Ramos wt and the PKCδ KO cell line (Fig. 1B). In this analysis we identified several serine residues in the N-terminal and C-terminal cytosolic tail of CD20 that are constitutively phosphorylated by PKCδ. Thus, PKCδ and CD20, two gatekeepers of the resting state of B lymphocytes, are connected by an enzyme/substrate relationship. Global serine/threonine phospho-proteome analysis of Ramos wt and PKCδ KO cells also reveal specific alterations in the phosphorylation of components of the RhoA/Rock-1 pathway and the MT cytoskeletal network described below (Fig. S1C). A comparison of the RNA-seq data obtained from the two cell lines indicated that, compared to Ramos wt, the PKCδ KO cells displayed an increased expression of genes encoding for proteins involved in MT depolymerization and a loss of cortical cytoskeletal stability (Fig. S2A and S2B).

118

119 **CD32b is associated with the IgD-BCR nanocluster and stabilizes CD20 expression**

120 The 20-fold upregulation of CD32b on the surface of PKCδ KO Ramos B cells suggests that
121 this inhibitory Fc receptor also has a constitutive gatekeeper function for the resting B cell
122 stage[26]. To test for this, we generated Ramos clones with a CD32b deficiency (CD32b KO) or
123 CD32b overexpression (CD32b-tr). Ramos wt cells express very low amounts of CD32b on
124 their surface, but the CD32b KO line clearly showed that this level can be further reduced to
125 background levels (Fig. 2A). Transfection of Ramos B cells with a human CD32b lentiviral
126 expression vector resulted in a 500-fold increase of CD32b on the surface of CD32b-tr Ramos
127 cells (Fig. 2B). To test for alterations of B cell marker proteins on CD32b-deficient or -
128 overexpressing Ramos cells (CD32-tr), we directly compared these cells with Ramos wt cells
129 in a flow cytometric analysis. Loss of CD32b resulted in a reduced expression of proteins
130 associated with the IgD-class nanocluster such as CD20, CD40, CXCR4, and the IgD-BCR,
131 and a higher expression of CD19 and the IgM-BCR, as well as the B cell activation marker
132 CD69 (Fig. 2C). Notably, CD19 and the IgM-BCR interact with each other on activated B
133 lymphocytes and the expression pattern on CD32b KO Ramos cells suggests that the loss of
134 CD32b results in a partial B cell activation[27]. The comparison of CD32b-tr to Ramos wt cells
135 shows an opposite phenotype, namely the increased expression of proteins associated with
136 the IgD-class nanocluster (Fig. 2D). The effect of the CD32b expression on the stability of the
137 IgD-class nanocluster suggests that CD32b is part of this membrane nanocluster. To test for
138 this, we employed the Fab-based proximity ligation assay (Fab-PLA), which monitors the 10-
139 20 nanometer proximity between the IgD-BCR and CD32b on the cell surface (Fig. 2E and
140 2F)[28]. The IgD:CD32b PLA signal monitored from Ramos wt is drastically increased upon
141 CD32b overexpression in CD32-tr, reaching a level that is similar to the PLA signal monitored
142 by human healthy donor (HD) B cells. As a negative control for this analysis, we tested Ramos
143 CD32b KO cells, which show no PLA signal. The comparable IgD-BCR/CD32b PLA signal
144 obtained from the analysis of CD32b-tr and HD B cells suggests a similar expression of CD32b
145 on these two cell types. This was verified by a comparative flow cytometry analysis of Ramos
146 CD32b-tr and HD B cells that also confirmed the higher CD20 expression on the Ramos
147 CD32b-tr B cells (Fig. S3). Because of these features and the more stable IgD-class
148 nanocluster we chose CD32b-tr Ramos B cells for our further studies of the cellular function of
149 CD20.

150

151 **Function of CD20 serine residues and their association with 14-3-3 adaptor proteins**

152 The serine/threonine phosphoproteome analysis of Ramos and its PKCδ-deficient subclones
153 suggests that 4 serine residues in the N-terminal cytosolic tail (S7, S35/36, S49) and 3 serine
154 residues in the C-terminal cytosolic tail (S225, S253/254) of CD20 are constitutively
155 phosphorylated by PKCδ. Interestingly, the three most significant CD20 serine phosphorylation
156 sites (S35/36, S225) are found in the context of an RxxS motif that, once phosphorylated,

157 could become a binding target of the 14-3-3 adaptor family members, which function by binding
158 to serine/threonine-phosphorylated intracellular proteins and altering the conformation,
159 activity, and subcellular localization of their binding partners (Fig. 3A)[29–31]. Additionally, another
160 serine residue (S221) is located near the plasma membrane. Neither the phosphorylated nor
161 the unphosphorylated form of S221 was detected in the phosphoproteome, perhaps because
162 of an adjacent palmitoylation at C220[32]. S221 lies within a classical RxxSxP binding motif for
163 14-3-3. To eliminate all possibilities of 14-3-3 binding, S221 was also mutated to alanine. To
164 test for the function of the identified serine residues, we generated expression vectors for WT
165 or mutant CD20 proteins carrying a serine to alanine (S/A) exchange of either the 4 N-terminal
166 (Nmut), the 4 C-terminal (Cmut), or all 8 serine residues (NCmut). For purification purposes,
167 the expressed CD20 proteins also carry a C-terminal flag-tag (Fig. 3B). Next, we employed the
168 CRISPR/Cas-9 method to generate CD20-deficient Ramos B cells that were transfected with
169 retroviral expression vectors encoding either CD20 WT or tail mutants (Nmut, Cmut, or NCmut)
170 of CD20. The obtained CD20 transfectants were sorted and further transfected with the human
171 CD32b lentiviral expression vector. Flow cytometry analysis showed that all four double-
172 transfectants expressed CD20 and CD32b at levels similar to the CD32b-tr Ramos line (Fig.
173 3C). A similar expression was also found for CD19 as well as the IgM- and IgD-BCR. However,
174 in comparison to the CD32b-tr Ramos line and the CD20 WT transfectants, Ramos cells
175 expressing the Nmut, Cmut, or NCmut CD20 mutant displayed a higher expression of the
176 activation marker CD83 suggesting that the S/A exchange partially compromises the
177 gatekeeper function of CD20 (Fig. 3C, far right)[33].
178 The finding that 4 of the 8 serine residues under study are part of an RxxS motif sequence
179 suggests that CD20 is not only constitutively phosphorylated by PKCδ but also constitutively
180 associated with a 14-3-3 adaptor protein. To test for this, we used the 1-PLA assay to monitor
181 the colocalization of CD20 with a 14-3-3 adaptor protein in CD32b-tr Ramos cells and
182 CD32b/CD20 double-transfectants expressing in addition to CD32b, either CD20 WT or one
183 of three different tail mutants of CD20 (Fig. 3D and 3E). The 1-PLA assay employs CD20 and
184 14-3-3 specific DNA-coupled antibodies that detect a colocalization of the two proteins in the
185 10-40 nanometer range[28]. A colocalization of CD20 with 14-3-3 is detected in the CD20 WT,
186 but to a lesser extent in the CD20 Nmut, Cmut or NCmut Ramos cells. Western blot analysis
187 of anti-flag immunoprecipitates of Ramos cell lysates confirms that, compared to CD20 WT,
188 the S/A mutants of CD20 are less well associated with the 29 kD 14-3-3 protein (Fig. 3F).
189
190 **The GEF-H1 activity is regulated by the cytoplasmic tails of CD20**
191 14-3-3 is a dimeric adaptor protein that can stabilize a CD20 homodimer and/or the
192 heterodimeric association of CD20 with other RxxS motif-containing proteins. In a preliminary
193 study, we found that exposure of B cells to anti-CD20 antibodies activates the RhoA/Rock1
194 signaling pathway (see below). A key activator of this pathway is the GDP/GTP exchange
195 protein GEF-H1 (also known as ARHGEF2), which is constitutively associated with the MT

196 network in resting B cells[34–39]. The intrinsically disordered regions in the C-terminal tail of GEF-
197 H1[35] carries an RRxxR and an RxxSxP motif (Fig. 4A). The RRxxR motif is a known binding
198 target for light chains of the dynein motor complex (such as LC8 or Tctex-1) and is thought to
199 be one of the interfaces linking GEF-H1 to MTs[37]. The serine residue S886 within the RxxSxP
200 motif of GEF-H1 is phosphorylated by the p21-activated kinase-2 (PAK2), a modification that
201 is known to inhibit GEF-H1 activity[40]. Binding of a 14-3-3 adaptor protein to the phosphorylated
202 RxxSxP motif may connect GEF-H1 to the constitutively phosphorylated CD20 tails. To test
203 for this, we used the 1-PLA assay and found a colocalization of CD20 and GEF-H1 in the CD20
204 WT transfectant and to a lesser extent in the CD20 Nmut, Cmut or NCmut transfected Ramos
205 cells (Fig. 4B and 4C). Western blot analysis of anti-flag immunoprecipitates of CD20 proteins
206 in the Ramos cell lysates confirmed that the tail mutants of CD20 are less well associated with
207 GEF-H1 than CD20 WT (Fig. 4D). In particular, the NC double-mutant of CD20 is hardly
208 associated with GEF-H1, compared to CD20 WT.
209 The amount of the GDP/GTP exchange active GEF-H1 protein in the cytosol of Ramos B cells
210 can be tested by a pulldown assay employing a G17A trapping mutant of RhoA, which
211 stabilizes the intermediate RhoA/GEF-H1 interaction[41]. For this, lysates of the different Ramos
212 cell lines were incubated with GST-RhoA-G17A-coupled GST beads, and the bound GEF-H1
213 was monitored by western blotting. Compared to CD20 WT, the cytosol of Ramos cells
214 expressing the Nmut, Cmut or NCmut contains a higher amount of active GEF-H1/RhoA
215 complexes (Fig. 4E and 4F). Taken together, these data suggest that the constitutively
216 phosphorylated serine residues within the cytosolic tails of CD20 regulate the RhoA/Rock-1
217 pathway via the binding and sequestering of GEF-H1.
218
219 **Exposure to anti-CD20 antibody activates the RhoA/Rock-1 pathway**
220 We next asked whether or not the exposure of Ramos B cells to a therapeutic anti-CD20
221 antibody such as rituximab (RTX) alters the interaction of CD20 with components of the
222 RhoA/Rock-1 pathway. For this we employed the 1-PLA assays to monitor changes in the
223 proximity of CD20 to 14-3-3, GEF-H1, RhoA and Rock-1 in Ramos CD32b-tr as well as CD20
224 WT or CD20 NCmut transfectants before or after a 5 min exposure to RTX (Fig. 5). The RTX
225 treatment reduced the CD20/14-3-3 proximity in CD32b-tr and CD20 WT transfected Ramos
226 cells to the level of unstimulated NCmut Ramos cells (Fig. 5A and 5B) and the same was found
227 for the CD20/GEF-H1 proximity (Fig. 5C and 5D). Interestingly, the 1-PLA assays show an
228 increased proximity of CD20 and RhoA (Fig. 5E and 5F) as well as CD20 and Rock-1 in RTX-
229 treated Ramos cells expressing CD20 WT but not those expressing CD20 NCmut. This study
230 suggests that in RTX-treated B cells, CD20 stabilizes a RhoA/Rock-1 complex at the inner
231 leaflet of the plasma membrane in a 14-3-3-dependent manner[42,43]. Importantly, the C-
232 terminus of Rock-1 also carries an evolutionary conserved RxxS motif. Thus, it is feasible that
233 CD20 functions not only as a gatekeeper of the resting state, but also as a switch that promotes
234 activation of the RhoA/Rock-1 pathway in antigen- or RTX-exposed B cells. As a control, we

235 determined whether active GEF-H1 is formed after RTX activation following GDP/GTP
236 exchange. The pull-down assay with the G17A trapping mutant of RhoA shows an increase in
237 active GEF-H1/RhoA complexes, especially in Ramos, CD32b-tr and WT cells (Fig. S4A and
238 4B).
239 We then used the phosphoflow assays to monitor alteration in the phosphorylation of members
240 of the RhoA/Rock-1 pathway after the RTX treatment of CD32b-tr, CD20 WT or NCmut Ramos
241 cells (Fig. S5). Exposure of CD32b-tr or CD20 WT Ramos cells to RTX results in a reduction
242 of the S886 phosphorylation of GEF-H1 and the loss of the inhibitory S188 phosphorylation of
243 RhoA (Fig. S5A and 5B). The same treatment resulted in an increased phosphorylation of
244 tyrosine Y914 of Rock-1, a modification that is associated with Rock-1 activation (Fig.
245 S5C)[44,45]. Importantly, all these amino acids are less well phosphorylated in the NCmut Ramos
246 cells and their phosphorylation state is not significantly altered after exposure of the cells to
247 RTX. Together these data demonstrate that the cytosolic serine/threonine residues studied
248 connect CD20 to the RhoA/Rock-1 signaling pathway.
249 Exposure to the therapeutic antibody RTX activates the RhoA/Rock-1 signaling pathway not
250 only in Ramos but also naïve human B cells. This is indicated by the time-dependent alteration
251 of the phosphorylation status of GEF-H1, RhoA and Rock-1 upon the treatment of HD B cells
252 with 10 ug/mL of RTX (Fig. S5D-5F). The 1-PLA assays of HD B cells before or after a 5 min
253 exposure to RTX show a reduction of the 14-3-3 (Fig. 6A and 6B) and GEF-H1 (Fig. 6C and
254 6D) proximity to CD20 and at the same time a strong recruitment of RhoA (Fig. 6E and 6F)
255 and Rock-1 (Fig. 6G and 6H) in the vicinity of CD20 in the RTX-treated cells. Thus, the CD20
256 engagement not only liberates and activates GEF-H1 but also results in an increased coupling
257 of the engaged CD20 to the RhoA/Rock-1 signaling module. Interestingly not only the RTX
258 treatment but also exposure of HD B cells to a MT polymerization inhibitor such as nocodazole
259 (Noc) changes the CD20 association with components of the RhoA/Rock-1 signaling pathway
260 (Fig. 6E-6H).
261
262 **Destabilization of MTs and the IgD-BCR nanocluster by anti-CD20 antibodies**
263 It is well known that GEF-H1 is associated with the MT network and that MT destabilization
264 results of GEF-H1 liberation and increased activity[34,36–38,46,47]. The result of our 1-PLA assay
265 (see above) suggests that the activation of RhoA/Rock-1 signaling pathway by RTX is
266 mediated by the destabilization of the MT cytoskeleton. To test for this, we pretreated HD B
267 cells for 1 hour with either Noc or with the MT stabilizer docetaxel (Tax) and then measured
268 RTX-induced changes by flow cytometry (Fig. 7A and 7B). The RTX-induced reduction of
269 CD20 abundance and the increased Rock1 phosphorylation can be prevented by pretreating
270 the HD B cells for 1 hour with Tax, whereas the Noc-pretreated HD B cells show already an
271 Rock1 activation with no further increase by RTX. Thus, the immediate effect of the binding of
272 RTX to CD20 seems to be the destabilization of the MT network resulting in GEF-H1 liberation
273 and the activation of the RhoA/Rock-1 signaling pathway.

274 MT dynamics are tightly regulated. To test whether binding of RTX to CD20 can influence or
275 induce the destabilization of MTs, Ramos CD32b-tr cells were treated with RTX and labeled
276 with mouse anti-alpha-tubulin to visualize tubulin structures by immunofluorescence
277 microscopy. In the Airyscan Super-Resolution (SR) imaging results (Fig. S6) we could visualize
278 the peeling of MT polymers, the outwardly curved spiral protofilaments at the end of shortening
279 MT upon RTX exposure (Fig. S6A and B). In a second approach with HD naïve B cells (Fig.
280 S7A-C), Airyscan (SR) confocal images of the labeled α-tubulin showed a spatial distribution
281 of small "ram's-horn" MT intermediates upon RTX treatment (Fig. S7B)[48,49]. Interestingly, a
282 pretreatment with Tax before RTX exposure could stabilize the B cell integrity and reduce MT
283 depolymerization (Fig. S7C).
284 On resting B cells CD20 and CD19 reside in the same protein/lipid nanocluster in close
285 proximity to the IgD-BCR, and the exposure to RTX leads to IgD-BCR/CD19 dissociation and
286 the formation of an IgM-BCR/CD19 complex[21]. Taking advantage of the Fab-PLA technique,
287 we next asked whether or not the MT network is involved in the nanoscale receptor
288 organization and reformation. Indeed, the exposure of the HD B cells to either RTX or Noc
289 results in a dissolution of the IgD-BCR nanocluster and IgM-BCR/CD19 conjugation. The RTX-
290 induced nanoscale receptor rearrangements are partially prevented by the pretreatment of the
291 HD B cells with Tax (Fig. 7C-7F). Taken together, these data show that in resting B cells the
292 nanocluster of the IgD-BCR is connected to the MT network and that the cytosolic tails of CD20
293 play an important role in this connection and its formation.
294
295 **Discussion**
296
297 **PKCδ and CD20: a kinase/substrate pair with a gatekeeper function**
298 We previously have shown that CD20 is stabilizing the membrane nanocluster of the IgD-BCR
299 and acts as a gatekeeper for the resting state of B lymphocytes[21]. Here we describe that serine
300 residues within the cytoplasmic tails of CD20 play an important role for this gatekeeper
301 function. Specifically, we show that 6 serine residues of CD20 are constitutively
302 phosphorylated by the serine/threonine kinase PKCδ and that this modification couples CD20
303 to the MT network in resting and the RhoA/ROCK1 signaling pathway in activated B cells. The
304 exchange of the serine to alanine residues did not alter the amount of CD20 on the B cell
305 surface, but it has an impact on the B cell activation state as the CD20 mutated Ramos cells
306 displayed a higher expression of the CD83 activation marker[33]. These data suggest that the
307 phosphorylated serine residues are connected to the gatekeeper function of CD20. The notion
308 that PKCδ also acts as a gatekeeper for the resting state of B lymphocytes is supported by
309 several genetic data[22,24,50,51]. The PKCδ KO mice develop autoimmunity[52] and loss-of-function
310 mutations of PKCδ in humans are associated with autoimmune diseases such as systemic
311 lupus erythematosus (SLE) or a B cell lymphoproliferative syndrome[53]. Our finding that CD20

312 is a substrate of PKCδ provides a novel mechanistic insight in the development of these
313 autoimmune diseases.
314 PKCδ has multiple substrates at the membrane, in the cytosol and inside the nucleus[50]. Thus,
315 the targeting of PKCδ to a specific subcellular location may determine its biological function in
316 different settings. Like many other kinases, PKCδ is regulated by an autoinhibitory mechanism
317 where the N-terminal regulatory domain is folded over the C-terminal catalytic domain, thus
318 inhibiting the kinase activity. The specific targeting of PKCδ is connected with an opening of
319 the autoinhibited conformation and kinase activation. For example, the binding of the N-
320 terminal C1A/B domain to diacylglycerol (DAG) recruits the open, active form of PKCδ to the
321 plasma membrane[54]. The location and activity of PKCδ can also be regulated by
322 posttranslational modifications. Interestingly, the SRC-family kinase Lyn can phosphorylate
323 and bind to tyrosine 52 of PKCδ[55,56]. The formation of the Lyn/PKCδ complex activates both
324 kinases and places them at the inner leaflet of the plasma membrane. We have previously
325 found that, after an Igα phosphorylation, the IgD-BCR is associated with PKCδ[24]. It is thus
326 feasible that an active Lyn/PKCδ complex is formed within the IgD-BCR nanocluster, thereby
327 explaining the constitutive serine phosphorylation of CD20 at this location.
328
329 **CD20 binds GEF-H1 and inhibits the GDP/GTP exchange activity in resting B cells**
330 Four of the 8 mutated serine residues of CD20 are part of conserved RxxS or RxxSxP motifs
331 that are well-known binding sites for 14-3-3 adaptor proteins[57]. A constitutive CD20/14-3-3
332 association in resting human B cells was confirmed by a 1-PLA and immune precipitation. The
333 RxxS and RxxSxP sequence is localized at the CD20 N-terminus and C-terminus, respectively.
334 The binding of the dimeric 14-3-3 adaptor to these sequences can either alter the
335 intramolecular conformation of the two cytosolic tails of CD20 or stabilize the formation of a
336 CD20 homodimer. Alternatively, the 14-3-3 dimer could also connect CD20 to other signaling
337 molecules[58,59]. Using a 1-PLA and immune precipitation assays we confirmed that the
338 GDP/GTP exchange factor GEF-H1, which carries a conserved RxxSxP motif at its
339 unstructured C-terminus, is one of the binding partners of the constitutively phosphorylated
340 CD20. The serine residue S886 within the conserved RxxSxP motif of GEF-H1 is constitutively
341 phosphorylated by Pak2, a modification that is associated with the inhibition of the GDP/GTP
342 exchange activity[60]. Thus, two serine/threonine kinases, PKCδ and Pak2, control the formation
343 and silencing of the CD20/GEF-H1 complex.
344 The activity of GEF-H1 is regulated by the cytoskeleton[47]. Specifically, GEF-H1 is intimately
345 associated with the MT network and this association inhibits its GDP/GTP exchange activity.
346 There are two (non-mutually exclusive) mechanisms how MT binding inhibits GEF-H1. In the
347 first one, polymerized MT stabilize the autoinhibited conformation in which the N-terminal C1
348 domain is folded over the PH domain of GEF-H1[61]. The second mechanism involves the
349 binding of the light chain protein Tctex-1 of the dynein motor complex to the RRxxR binding

350 motif at the unstructured C-terminal tail of GEF-H1[62,63]. In this way the dimeric dynein motor
351 complex couples GEF-H1 to polymerized MT. The RxxSxP motif that connects GEF-H1 to the
352 phosphorylated CD20 tails lies 60 amino acids downstream of the Tctex-1 binding site. Thus,
353 in resting B cells the autoinhibited GDP/GTP exchange factor functions as an adaptor that
354 connects CD20 to the MT network. Based on the finding that anti-CD20 antibodies can
355 modulate the calcium response in B lymphocytes, it has previously been suggested that CD20
356 acts as a calcium channel[64,65]. This suggestion is not supported by the CD20 structure which
357 did not reveal a calcium permeable pore[7]. However, we noticed that the N-terminus of the
358 store-operated calcium channel ORAI 1 carries an RRxxR and an RxxS motif[66]. Thus, Tctex-
359 1 and the 14-3-3 adaptor could couple CD20 to the ORAI1 channel and this connection could
360 explain the observed effect of anti-CD20 antibodies on the calcium response in B lymphocytes.
361
362 **CD20 can orchestrate the MT-to-actin switch during B cell activation**
363 In migrating, polarized B lymphocytes, the MT organization center (MTOC) is found in the
364 vicinity of the trailing edge and the MT network is involved in the organization of the uropod at
365 this location[67]. We have found that in polarized B cells the IgD-BCR nanocluster is localized at
366 the uropod whereas at the leading-edge the IgM-BCR is associated with microvilli structures
367 that are formed by core bundles of actin filaments[68]. The interaction of CD20 to the MT network
368 may help to stabilize the IgD-BCR nanocluster[69]. Interestingly, apart from the CD20/GEF-H1
369 complex the IgD-BCR nanocluster harbors several receptors that carry in their cytosolic
370 juxtamembrane region a RRxxR (BAFF-R) or a related RRxxK motif (CD19) for Tctex-1
371 binding. Thus, multiple contact points to the MT network may promote the stability of the IgD-
372 BCR nanocluster[70].
373 In polarized lymphocytes RhoA and ROCK1 are also found at the uropod and a RhoA
374 deficiency or an inhibition of ROCK1 kinase activity prevents the formation of this structure[67,71].
375 RhoA undergoes geranylgeranylation at its C-terminal CAAX motif and thus is constitutively
376 bound via its lipid anchor to the inner leaflet of the plasma membrane[72]. In spite of its
377 permanent membrane association, RhoA in resting B cells is not found in the vicinity of CD20
378 and the IgD-BCR nanocluster as the PLA has shown. Only upon MT destabilization and the
379 following dissociation of the GEF-H1/CD20 complex RhoA and ROCK1 are found in the vicinity
380 of CD20. Interestingly, ROCK1 carries a RxxS motif close to its C-terminus and it is feasible
381 that the GEF-H1/CD20 complex in resting B cells is replaced by a RhoA-GTP/ROCK1/CD20
382 complex in activated B cells. The GEF-H1 activation and liberation from the MT network could
383 have a dual impact on ROCK1 activity and membrane location. The increased GDP/GTP
384 exchange activity of GEF-H1 generates RhoA-GTP that attaches to the RhoA binding domain
385 of ROCK1 and the GEF-H1-deprived CD20/14-3-3 complex is free to bind to ROCK1. Both
386 binding events counteract ROCK1 autoinhibition and localizes the active ROCK1 at the IgD-
387 BCR nanocluster where ROCK1 phosphorylates the myosin light chain (among other
388 substrates), resulting in the formation of myosin-II filaments and actomyosin stress fibers with

389 increased contractility[73]. The stress fiber formation in polarized, antigen-exposed activated B
390 cells[58,74] may be associated with uropod retraction, the dissociation of the IgD-BCR
391 nanocluster and the observed movement of CD20 and CD19 to the IgM-BCR. According to
392 this scenario CD20 is not only a gatekeeper of the resting state but also an actomyosin bundles
393 associated transporter that promotes the immunoreceptor coupling and organization motif
394 (ICOM)-dependent conjugation of the IgM-BCR with the CD19 coreceptors in activated B
395 lymphocytes[75].
396
397 **The effect of anti-CD20 antibodies on cytoskeleton reorganization**
398 Previously it was thought that binding of anti-CD20 antibodies did not have a direct effect on
399 the physiology of targeted B cells, but simply provided a flag for their destruction via
400 phagocytosis or ADCC mechanisms[76]. However, several studies indicated that anti-CD20
401 antibodies induce an apoptosis program in the targeted B cells[77]. We found that exposing B
402 cells to anti-CD20 antibodies results in the dissolution of MTs and MT instability, which is
403 associated with apoptosis [38,44,78]. Furthermore, caspase 3, an important effector of the
404 apoptosis program, can cleave and activate ROCK1[44]. Interestingly, it is the cleaved, active
405 ROCK1 fragment, which carries the C-terminal RxxS motif and therefore could still be
406 associated with CD20. In this way the active kinase domain of ROCK1 remains bound to the
407 plasma membrane in a RhoA-GTP independent manner. A recent 3-dimensional super-
408 resolution study has localized the RTX-engaged CD20 on actin bundles within microvilli
409 structures[79]. This is in line with our findings that the IgM-BCR is associated with an actin-based
410 network of ridges of microvilli structures and that CD20 is found in the vicinity of the IgM BCR
411 after exposure to either cognate antigen or anti-CD20 antibodies[68]. Together these data
412 support the assignment of CD20 as a switch factor, flexible to interact with the MT and
413 alternatively the actomyosin cytoskeleton in resting and activated B lymphocytes, respectively.
414 The finding that the exposure to anti-CD20 antibodies results in dissolution of MT bundles and
415 protofilaments and that MT-destabilizing drugs can mimic the effect of an anti-CD20 treatment
416 of B lymphocytes not only gives a new insight in the therapeutic effect of the anti-CD20 therapy
417 but also could have an impact on the improvement of such a therapy. It is known that anti-
418 CD20 treatment results in the reduction of the amount of CD20 on the B cell surface and this
419 could reduce the targeting efficiency[80,81]. The exposure of healthy donor B cells to MT
420 stabilizing drugs such a Taxol derivates could prevent the downregulation of antibody-bound
421 CD20 and thus increase the B cell targeting function of the anti-CD20 therapy. However, there
422 also exist data showing that the ADCC-dependent killing of anti-CD20 labelled B cells by NK
423 cells requires dynamic alterations of the MT network. If this is the case, a combination of anti-
424 CD20 therapy with MT-destabilizing drugs such a vincristine could enhance the NK-mediated
425 cytotoxicity of anti-CD20-targeted B cells[82]. While these potential modification of the anti-CD20
426 therapy requires more studies, the cellular function of CD20 as an adaptor between antigen

427 receptors and the cytoskeleton is now established and CD20 is no longer an enigma of B cell
428 biology.
429
430 **Materials & Methods**
431
432 **Human naïve B cells**
433 Primary naïve B cells were obtained from fresh buffy coats, provided by the Institute for
434 Transfusion Medicine and Gene Therapy, ITG, Freiburg. Peripheral blood mononuclear cells
435 (PBMCs) were separated by Ficoll gradient centrifugation of whole blood and negatively
436 selected using EasySep Human Naïve B Cell Isolation Kit (Stemcell). Prior to experiments,
437 primary B cells were controlled for purity and rested overnight. The study was approved by the
438 Institutional Review Board of the University Freiburg (Ethical votes No 507/16 and 336/16).
439
440 **Cell culture**
441 The human Burkitt lymphoma B cell line Ramos was obtained from American Type Culture
442 Collection (ATCC, Ramos cat. CRL-1923, RRID: CVCL 1646) and stably transfected with
443 ecotropic receptor (EcoR) to allow murine retroviral transfection with MMLV particles. Ramos
444 B cells were cultured in RPMI 1640-Glutamaxx medium, 10% FCS (PAN, Biotech), 10 units/mL
445 penicillin/streptomycin (Gibco), 20 mM hepes (Gibco), and 50 mM β-mercapto-ethanol (Sigma)
446 in a humidified saturated atmosphere at 37 °C with 5% CO_2.
447 For the quantitative phosphoproteomic study, Ramos B cells were labelled using stable isotype
448 labelling by amino acids in cell culture (SILAC). Light labelling was performed using 12C6L-
449 arginine/12C6-L-lysine. For medium-heavy and heavy labelling 13C6L-arginine/D4-L-lysine
450 and 13C615N4-L-arginine/13C615N2-L-lysine were used, respectively.
451
452 **Generation of the Ramos CD32b KO and CD20 KO cell lines**
453 The human CD32b and CD20 gene were render defective in the Ramos B cell system by the
454 CRISPR/Cas9 technique using the SgRNAs agcacgttgatccactgggg for CD32b KO (ex4) and
455 gccctattgctatgcaatctgg for the CD20 KO (ex3), respectively. The Neon Transfection System
456 (Invitrogen) was used to introduced a ribonucleoprotein (RNP) complex with the pre-
457 assembled Cas9 protein and guide RNA into the Ramos B cells according to the genome
458 editing method of Integrated DNA Technology (IDT). In brief: Ramos cell medium was changed
459 the day before transfection. 1×10^6 Ramos cells were pelleted by centrifugation and
460 resuspended in 9 µL buffer R (Neon), 1µL of RNP complex, and 2µL of electroporation
461 enhancer (IDT). RNP complex contained diluted sgRNA (annealed crRNA and tracrRNA in a
462 1:1 ratio in IDTE buffer) and Cas9 endonuclease in buffer R (NEON). Electroporation was
463 performed in 10 µL NEON tips at 1350 V, 30 ms, single pulse. The transfected cells were first
464 recovered for 72hs at 37°C and 5% CO2 without antibiotics and then subjected to complete
465 RPMI medium. Successful transfected Ramos cells were batch sorted using BioRad cell sorter

466 in three different rounds and monitored throughout experiments. Deletion of the target gene
467 was verified by flow cytometry.
468
469 **Generation of the Ramos PKCδ (PRKCD) gene KO**
470 The sequence AACCCAATCATAGCAGAGC or GCTGAGTTCAGTGAGTGC encoding for the
471 specific gRNA was inserted into a lentivirus CRISPR vector (Addgene). The constructs were
472 co-transfected with an mCherry expression vector into Ramos cells. The cells were incubated
473 at 37°C for 24 hours in a humidified CO2 incubator. The following day, single cells were sorted
474 for mCherry reporter gene expression with the BD FACSAria™ III Cell Sorter. The sorted single
475 cells were cultured for 3-4 weeks in complete RPMI medium supplied with 10% FBS in a
476 humidified CO_2 incubator at 37°C. The expected PRKCD gene deficiency was verified by
477 Sanger sequencing and the loss of PKCδ protein expression by Western blotting.
478
479 **Lentiviral transfection for the generation of CD32b-tr Ramos B cells**
480 The human embryonic kidney HEK 293T cells were cultured in complete DMEM GlutaMAX
481 medium supplemented with 10% FCS, 10 mM HEPES, 10 µM sodium pyruvate, 50 units/mL
482 penicillin and 50 µg/mL streptomycin in a humidified saturated atmosphere at 37 °C with 7.5%
483 CO_2. Lentivirus particles were obtained by co-transfecting HEK 293T cells with pLenti-
484 hCD32b-IRES-GFP, pCMVΔR8.74 and pMD2vsvG plasmids using Polyethyleneimine (PEI,
485 Polysciences). Viral supernatant was harvested, sterile filtered and combined 24h and 48h
486 post-transfection. Lentiviral particles were enriched by centrifugation (4 hs, 10.000 g, 8 °C)
487 after placing them in a 1:5 ratio on a 10% sucrose layer. The lentiviral pellet was resuspended
488 in DMEM Glutamaxx without supplements and stored at –80 °C. The viral titers were assessed
489 by determining the multiplicity of infection (MOI). Briefly, $5x10^4$ HEK 293T cells per well were
490 seeded in a p24 well plate in 1 mL medium. An aliquot of the concentrated virus was diluted
491 1:100 in medium. Various volumes (0, 1, 5, 10, 25, and 50 µL) of lentivirus dilution were added
492 to the cells. After 48h of incubation the GFP expression was analyzed by flow cytometry and
493 lentivirus titer was calculated: Transduction units/mL = (number of cells x % of GFP^+ cells x
494 dilution factor) / (mL of lentivirus dilution).
495
496 **Construction of WT or S/A mutated CD20-flag expression vectors**
497 The CD20-flag vector was modified by geneblocks (IDT) encoding the N-terminal or C-terminal
498 tails with S/A exchanges at the chosen 4 positions, respectively. Geneblocks were solved in
499 IDTE buffer according manufacturer's protocol and subsequently inserted in the pMIG CD20-
500 flag-IRES-GFP vector using infusion cloning method. Plasmid were sequenced (GATC,
501 eurofins) and used to generate the CD20WT, CD20Nmut, CD20Cmut and CD20NCmut
502 Ramos cell lines.
503
504 **Retroviral transfection of CD20 mutants:**

505 Murine retrovirus-containing supernatants were obtained by transfecting Phoenix-eco cells
506 with LipoJet (SignaGen) according to manufacturer's protocol and different pMIG-CD20-IRES-
507 GFP constructs, or empty GFP-control plasmid. After 48h viral supernatant was collected,
508 sterile filtered and used directly or stored in -80°C. For transduction $4x10^5$ newly generated
509 CD20 KO Ramos cells were resuspended in 1 mL of viral supernatant containing Polybrene
510 (1 µg/mL) and spin infected by centrifugation (180 min, 300g, 37°C). The viral supernatant was
511 removed and cells were cultured and sorted for GFP expression (BioRad cell sorter).
512

513 **RNA sequencing**

514 Wildtype Ramos or PRKCD Knockout Ramos were cultured with or without IgM (10ug/ml)
515 stimulation for 4 hours and then RNAs were extracted by RNeasy plus kit (Qiagen cat# 74143).
516 RNA libraries for RNAseq were prepared using the NEBNext® Ultra™ II Directional RNA
517 Library Prep Kit for Illumina (NEB cat # E7760L) according to manufacturer's instructions and
518 samples were sequenced 84-bases long on the NextSeq® 550 with high output flowcell
519 (NextSeq® 500/550 High Output Kit v2).
520

521 **GEO data**

522 Downstream analyses were conducted using R (version 4.4.0). Raw read counts were
523 normalized for library size and composition using the trimmed mean of M-values (TMM)
524 method. Differential gene expression analysis comparing the unstimulated Ramos and PKCδ
525 KO cell conditions was performed with the edgeR package (version 4.2.2)[83]. Gene set
526 enrichment analysis was carried out using the clusterProfiler package (version 4.12.6)[84]with
527 gene sets from the Molecular Signatures Database (MSigDB, version 7)[85]. For all statistical
528 analyses, significance was defined as an adjusted p-value < 0.05.
529

530 **Flow cytometry analysis and phospho-flow detection**

531 For surface staining, 1–20 x 10^5 cells were Fc-blocked (Human TruStain, Biolegend), stained
532 with fluorescent antibodies on ice, washed twice, and then their fluorescence measured with
533 a FACS Attune NxT (Life technologies). For intracellular staining and phospho-flow analysis,
534 the cells were activated for the requested time points, immediately fixed with 4% PFA, washed
535 twice and permeabilized with 0.5% saponin (Quillaja bark, Sigma) containing protease and
536 phosphatase inhibitors (HALT, Thermo Fisher) for 30 min. Samples were washed and stained
537 overnight at 4°C. If necessary secondary antibody staining was performed, the background
538 was controlled using only the secondary antibody. Data were exported in FCS-3.0 format and
539 analyzed with FlowJo software (TreeStar).
540

541 **Western Blotting**

542 Unstimulated or activated Ramos B cells were collected and immediately lysed in 2x Laemmli
543 or RIPA buffer for 30 min on ice. Equal amounts of adjusted and cleared lysates (Qubit 3.0;

544 life technologies) were subjected to SDS–PAGE on 10% mini precast gels (7bioscience). After
545 transfer, the PVDF membrane (GE Healthcare Amersham) was blocked with 5% BSA in PBS
546 and 0.1% Tween20. The membrane was first exposed to primary antibodies specific for the
547 proteins under study (CD20, 14-3-3 or GEF-H1) and then washed. A horseradish (HRP)
548 peroxidase-conjugated goat anti-rabbit or goat anti-mouse antibody was used as secondary
549 antibody before detection with ECL chemiluminescent substrate (Bio-Rad).
550
551 **Affinity purification of CD20-flag and GEF-H1**
552 The anti-flag immunoprecipitation was performed according to the manufacturer's protocol
553 (chromotek). In brief, 10^7 Ramos cells were lysed for 30 min in ice-cold lysis buffer
554 supplemented with a protease/phosphatase inhibitor cocktail (HALT, Thermo Fisher). Lysates
555 were centrifuged for 10 min at 17000 g and diluted in 300µL dilution buffer. 50 µL of total lysate
556 were kept for the input analysis. Diluted lysates were rotated overnight with anti-flag agarose
557 beads. Beads were then sedimented and washed extensively. Bound proteins were eluted with
558 2x SDS-PAGE Laemmli buffer and samples were boiled at 95°C for 5 min and subjected to
559 SDS-PAGE and Western blotting.
560 RhoA(G17A), the nucleotide-binding deficient mutant of RhoA binds strongly to GEF-H1 and
561 can be used for GEF-H1 purification and quantification. For this a glutathione S-transferase
562 (GST) coupled RhoA(G17A) fusion protein was produced in E. coli bacteria and the GST-
563 RhoA(G17A) loaded on Glutathione Sepharose beads. The GST-RhoA(G17A)-beads were
564 mixed with Ramos B cell lysate and rotated overnight at 4°C. Beads were washed extensively
565 with lysis buffer, boiled for 5 min and the cleared supernatant subjected to SDS-PAGE and
566 western blotting.
567
568 **Proximity ligation assay (PLA)**
569 The Fab-PLA was performed as described earlier[28]. In brief: for Fab-PLA, the F(ab)- fragments
570 were prepared from the corresponding antibodies using the Pierce Fab Micro Preparation Kit
571 (Thermo Fisher). The produced F(ab)-fragments or primary antibodies (1-PLA) coupled with
572 PLA probemaker (Sigma-Aldrich) after buffer exchange (Zeba™ spin desalting columns,
573 Thermo Fisher). Ramos or HD naïve B cells were settled on polytetrafluoroethylene (PTFE)
574 slides (Thermo Fisher Scientific) for 30 min at 37°C and kept unstimulated or activated with
575 RTX [10µg / mL] for 5 min and then fixed for 20 min with 4% paraformaldehyde.
576 After extensive washings the slides were blocked for 30 min with blocking buffer (25 µg/mL
577 sonicated salmon sperm DNA, 250 µg/mL BSA, 1 M glycine). PLA was performed with the
578 Duolink In Situ Orange (Sigma-Aldrich). Slides were directly mounted with DAPI Fluoromount-
579 G (Southern Biotech) to visualize the PLA signals in relation to the nuclei. For each experiment,
580 a minimum of 1000 HD B cells or Ramos cells were analyzed with CellProfiler-3.0.0. In brief:
581 metadata of images were exported and the intensity of the input frames were rescaled to the
582 full intensity range in the RGB scheme. PLA signals (size of PLAdots 4-10 pixels) in a distance

583 of 10 pixels to the Nuclei (size 15-80 pixel) with a threshold of 0.0075 of at least 1000 cells
584 were measured and subjected to analysis.
585
586 **Imaging, Image analysis, and Data processing**
587 All microscope images for PLA were acquired using Leica DMi8 microscope equipped with an
588 HC PL APO 63×/1.40-0.60 oil immersion objective lens and analyzed with CellProfiler 3.0.0.
589 and Prism software (GraphPad, La Jolla, CA).
590
591 **Microtubule staining**
592 MT were stained as described[86]. In brief: Ramos B cells were settled on uncoated glass bottom
593 chambers (IBIDI) for 30 min at 37°C, kept unstimulated or activated with RTX for 20 min and
594 then fixed for 20 min with 4% paraformaldehyde and 0.1% glutaraldehyde. After blocking and
595 permeabilization with 250 µg/mL BSA, 1 M glycine 0.5% saponine for 30 min cells were stained
596 with anti-α tubulin (Sigma Aldrich) over night and with secondary anti mouse Alexa fluor-555
597 antibody (Invitrogen). Fixed Ramos cells in IBIDI chambers were kept in PBS until microscope
598 imaging.
599 HD B cells were settled on PTFE slides (Thermo Fisher) for 30 min at 37°C, kept unstimulated,
600 or activated with RTX [10µg/mL] for 5 min, with or without pretreatment with Taxfor 1h and
601 then fixed for 20 min with 4% paraformaldehyde and 0.1% glutaraldehyde. After blocking and
602 permeabilization with 250 µg/mL BSA, 1 M glycine 0.5% saponine for 30 min cells were stained
603 with anti-α tubulin (Sigma Aldrich) over night and with secondary anti mouse Alexa fluor-555
604 antibody (Invitrogen). Slides were directly mounted with Fluoromount-G mounting-solution
605 (Invitrogen) and subjected to microscope analysis.
606
607 **Microscopy**
608 The high-resolution visualization of MTs was performed using a LSM 880 Airyscan laser
609 scanning confocal microscope attached to an inverted microscope Axio Observer Z1 (Carl
610 Zeiss Microscopy). The Alexa Fluor 555 labelled α-tubulin was excited with 561nm, the
611 emission was detected with the Airyscan detector in SuperResolution (SR) mode. For all cells
612 z-stacks were acquired with a Plan-Apochromat 63x/1.40 Oil DIC M27 (Fig. S7) or a LD LCI
613 Plan-Apochromat 40x/1.20 autocorr (Fig. S6) objective. The immersion medium was oil (63x)
614 or water (40x).
615 Zeiss Software ZEN Black 2.3 SP1 FP3 (release 14.0.22.201) was used for acquisition.
616 (acquisition settings for Fig. S7: EM filter SP615, pixel size xy:0.049µm, z-step size: 0.199µm,
617 pixel dwell time 1µs, bi-directional scanning, for Fig. S6: no EM filter, pixel size xy:0.049µm, z-
618 step size: 0.243µm or 1µm, pixel dwell time 1,92µs, bi-directional scanning). All images were
619 processed with the above ZEN Black software using the Airyscan algorithm and with Zen Blue
620 (Version 3.9.3) for subset and maximum intensity projection. Airyscan processed images
621 shown-in Fig. S6 are single z-planes from an image z-stack and in Fig. S7 maximum intensity

projections of the full image z-stack. The display gain is set to 0.75 and the intensity value to Best fit.

Statistical analysis

Students t-test was used for the experiments if not otherwise described to determine statistical significance provided by Prism10 software (GraphPad, La Jolla, CA).

MT network stabilization or destabilization

For the stabilization of MT HD naïve B cells or Ramos B cells were treated for 1 h with 100 nM docetaxel trihydrate (MedChemExpress) solved in DMSO and diluted in RPMI culture medium. For the destabilization of MT cells were treated for 1 h with 10 µM nocodazole (Selleck-Chemicals) solved in DMSO and diluted in RPMI culture medium.

Rituximab (RTX) treatment

RTX was kindly provided by F. Hoffmann-La Roche-AG. For naïve HD B cells or Ramos cell treatment RTX was diluted to a final concentration of 10 µg/mL and experiments were performed at least three times.

Phosphopeptide enrichment

SILAC-labeled Ramos B-cells (wild-type and knockout) were starved by serum depletion (FCS) for 30 min. Following starvation, cells were harvested by centrifugation at 1,200 rpm for 5 min, washed twice with starvation medium. As a control, mock treatment was performed using PBS. After activation, cells were rapidly snap-frozen in liquid nitrogen to preserve their signaling status. Cell lysis was performed using GdmHCl buffer (6 M GdmHCl, 100 mM Tris-HCl pH 8.5, 10 mM TCEP, and 40 mM chloroacetamide). The cell pellets were resuspended in the lysis buffer, followed by sonication (two cycles of 30 seconds). Protein denaturation was achieved by incubating the lysates at 95°C for 5 min. To remove cellular debris, the lysates were centrifuged at 3,500 x g for 30 min at 4°C. Protein concentration was determined using a Bradford assay. To precipitate proteins, four volumes of ice-cold acetone were added to the lysate. The protein precipitates were collected by centrifugation and washed with ice-cold acetone to remove residual contaminants. Proteins were digested using a combined Lys-C / trypsin digestion. Phosphopeptides were enriched using the Easyphos workflow. The phosphopeptide-enriched eluates were desalted using C18 StageTips (3M Company), pooled, and stored at -80°C until further analysis.

LC-MS/MS analysis

Peptide mixtures, reconstituted in 0.1% TFA, were analyzed by nano HPLC-ESI-MS/MS using an UltiMate 3000 RSLCnano HPLC system (Thermo Fisher Scientific, Dreieich, Germany) online coupled to an QExactive Plus mass spectrometer (Thermo Fisher Scientific, Bremen,

661 Germany). The RSLC system was equipped with C18 trap columns (nanoEase M/Z Symmetry
662 C18 Trap; 20 mm length, 180 µm inner diameter, 5 µm particle size, 100 Å pore size, Waters
663 Corporation, Milford, MA) and an analytical C18 reversed-phase nano LC column (nanoEase
664 M/Z HSS C18 T3; 250 mm length, 75 mm inner diameter, 1.8 µm particle size, 100 Å pore
665 size, Waters Corporation, Milford, MA). A binary solvent system consisting of 0.1% (v/v) formic
666 acid (FA) as solvent A and 80% (v/v) acetonitrile (ACN)/0.1% (v/v) FA as solvent B was
667 employed for peptide separation. Peptide mixtures were loaded, washed and preconcentrated
668 on the pre-column for 5 min using solvent A and a flow rate of 10 µL/min. A gradient was then
669 applied at a flow rate of 300 nL/min ranging from 4 to 39% B in 140 min, 39–54% B in 15 min,
670 54%-95% in 5 min and 3 min at 95% B. Eluted peptides were transferred to a fused silica
671 emitter for electrospray ionization enabled by a Nanospray Flex ion source with DirectJunction
672 adaptor (Thermo Fisher Scientific), applying a spray voltage of 1.6 kV and a capillary
673 temperature of 250°C. MS/MS data were acquired in data-dependent mode using the following
674 parameters: MS precursor scans at m/z 370–1700 with a resolution of 70,000 (at m/z 400);
675 automatic gain control (AGC) of 3×10^6 ions; a maximum injection time (IT) of 60 ms; a top 12
676 method for higher-energy collisional dissociation of multiply charged precursor ions with a
677 normalized collision energy of 28%. MS/MS scans from 200 to 2000 m/z were recorded at a
678 resolution of 35,000. The AGC for MS/MS scans was set to 1×10^5 with a maximum IT of 120
679 ms and a dynamic exclusion time of 45 s. Data are available via ProteomeXchange with
680 identifier PXD063667.
681
682 **MS data analysis**
683 MaxQuant (version 2.6.7.0) with its integrated Andromeda search engine[87,88] was employed.
684 MS/MS data were searched against the human proteome set with isoforms downloaded from
685 UniProt (105300 entries). Protein identification was performed using MaxQuant default
686 settings (including carbamidomethylation of cysteine residues as fixed modification and N-
687 terminal acetylation and methionine oxidation as variable modifications), with the following
688 exceptions: 'Arg6;Lys4' and 'Arg10;Lys8' were specified as medium and heavy modification
689 labels, respectively; a maximum of three missed cleavages was allowed; 'Phospho (STY)',
690 'Oxidation (M)' and 'Acetyl (Protein N-term)' were selected as variable modifications; and the
691 options 'match between runs' and 'requantify' were activated.
692 Ratios between labels (normalized by MaxQuant) were extracted from the
693 Phospho(STY)Sites.txt file, reverse entries and potential contaminants were removed, and the
694 list was filtered for at least two unique peptides per phosphosite. Phosphosite ratios were
695 normalized to the respective ratio at the protein group level using the median ratio of all protein
696 group ratios referenced in the 'Protein group IDs' column of the Phospho(STY)Sites.txt file.
697 Resulting phospho site ratios were filtered so that only sites with valid values in >=3 of 4
698 replicates were retained. Significance of differential regulation was tested using linear models
699 implemented in the LIMMA package and the resulting fold changes and significance level were

plotted. Data analysis was performed in Python 3.10 using the autoprot wrapper [89] for data analysis and plotting. All original code for MS data analysis has been deposited at Zenodo (https://doi.org/10.5281/zenodo.15350913).

Acknowledgments

We thank Dr. Christian Klein and the Roche Innovation Center Zurich for financial support and anti-CD20 antibodies and Falk Nimmerjahn, University of Erlangen for the CD32B plasmid. The generation of the CRISPR-Cas9 PKCδ plasmid and RNA sequencing was made possible by the help of Dr. Claudio Mussolino and Dr. Baerbel Keller. We thank them for their assistance. We thank Dr. Lise Leclercq for correcting the manuscript. We also thank the Lighthouse Core Facility, which is funded in part by the Medical Faculty, the University of Freiburg (Project Numbers 2023/A2-Fol; 2021/B3-Fol), the DKTK, and the DFG (Project Number 450392965).

Funding: This work was supported by the Roche research contract ZVK-2023101202 and an RO1 grant of the National Institutes of Health (NIH) under the award number A031503 (SMA, MR). The Zeiss LSM 880 microscope was funded by the Deutsche Forschungsgemeinschaft (DFG), Project No. 31778431, Work in the Warscheid lab was supported by the DFG SPP2453 (project number 541758684), FOR2743 (project 9) and TRR130 (project C01).

Disclosure and competing interest statement

The authors declare no conflict of interests.

Supplements

Main figures 1-7

Supplemental figures S1-S7

Structured Methods - Reagents and Tools Table

Extended table 1 Geneblocks

Graphical abstract

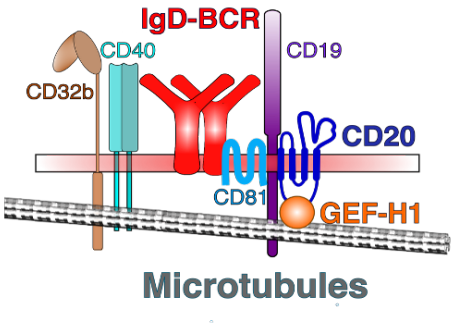

Scheme of the resting B cell IgD-BCR cluster connected to the microtubule network

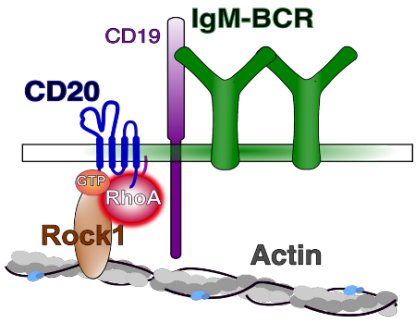

The activated B cell IgM-BCR connected by Rock1 to the actin network

Figure 1

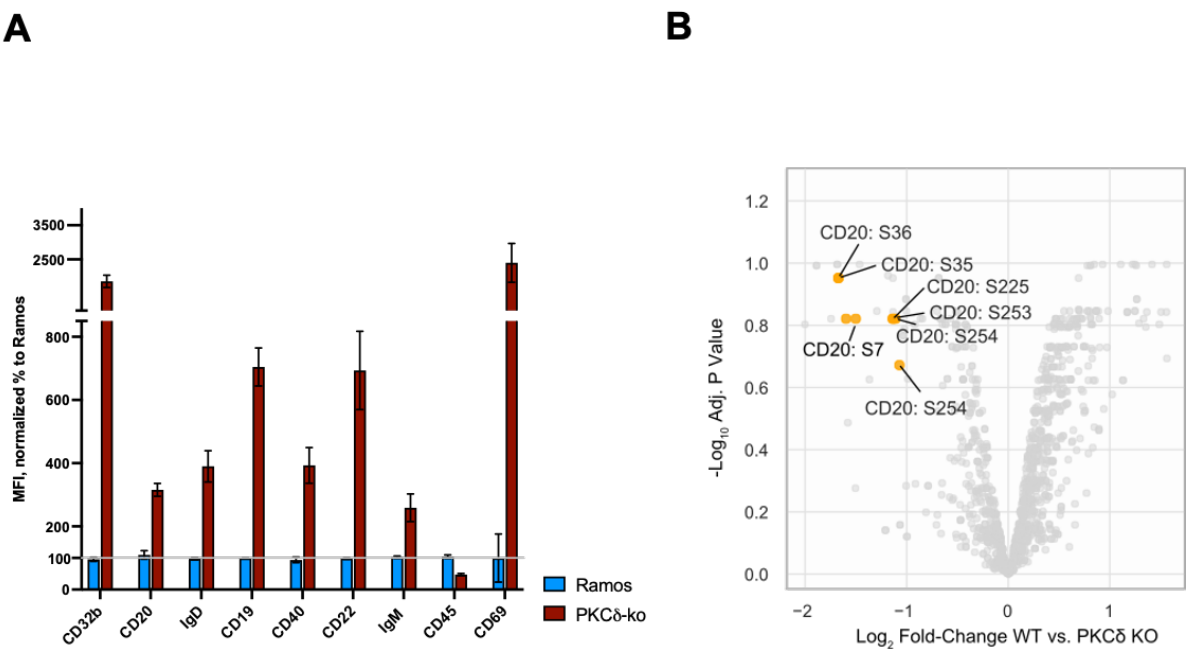

Figure 1:

Phenotype of PKCδ KO Ramos B cells and identification of PKCδ substrate proteins. Comparison of the expression of B cell marker protein on the surface of PKCδ KO (brown) and WT Ramos B cells (blue) by flow cytometry. The expression data of PKCδ KO are normalized to that of WT Ramos cells set to 100%. **B**. Volcano plot showing quantitative changes of the constitutive serine/threonine phosphorylation of substrate proteins of WT in comparison to PKCδ KO Ramos B cells. On the X-axis the plot depicts log2 fold change of phosphorylated serine or threonine residues in the whole proteome of the two cell lines. The Y-axis shows the log10 FDR adjusted p-value <0.05. The significant changes of phosphorylated CD20 serine residues are indicated and shown in orange.

Figure 2

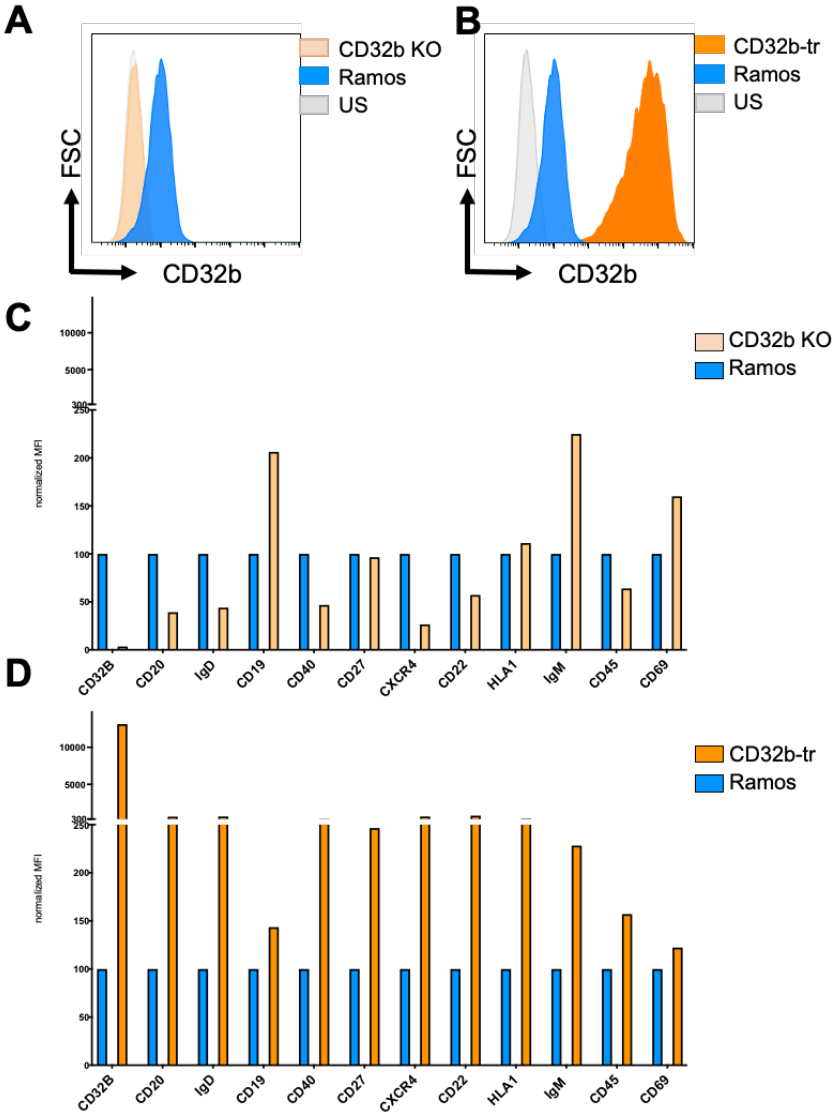
A
CD32b KO
Ramos
US
FSC
CD32b
B
CD32b-tr
Ramos
US
FSC
CD32b
C
CD32b KO
Ramos
normalized MFI
CD32B
CD20
IgD
CD19
CD40
CD27
CXCR4
CD22
HLA1
IgM
CD45
CD69
D
CD32b-tr
Ramos
normalized MFI
CD32B
CD20
IgD
CD19
CD40
CD27
CXCR4
CD22
HLA1
IgM
CD45
CD69

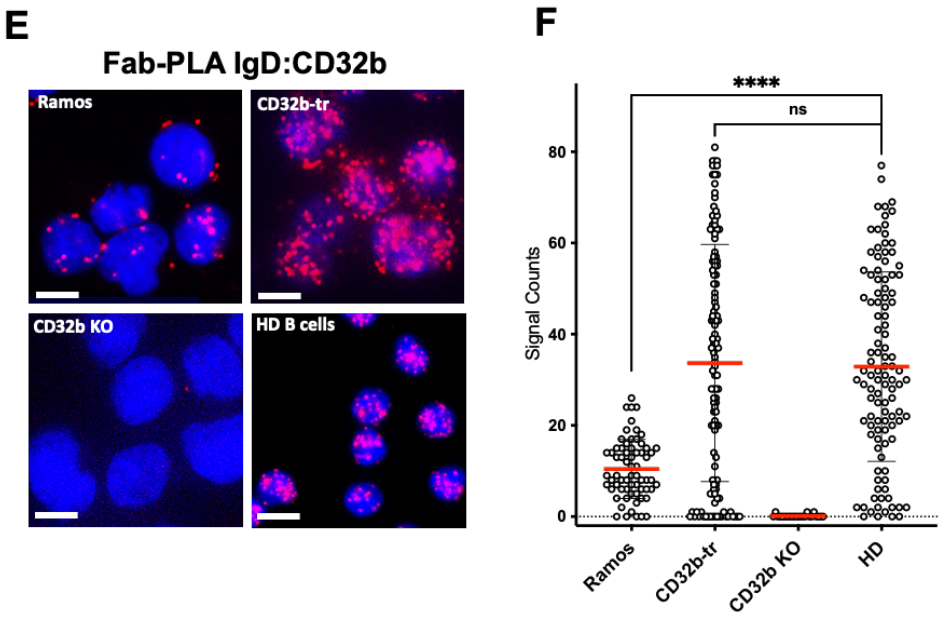
E
Fab-PLA IgD:CD32b
Ramos
CD32b-tr
CD32b KO
HD B cells
F
****
ns
Signal Counts
Ramos
CD32b-tr
CD32b KO
HD

Figure 2:

Functional association of the Fc-receptor CD32b with the IgD-BCR nanocluster.

A, B. Flow cytometry analysis of CD32b expression on the surface of CD32b KO (beige) or CD32b-tr (orange) in comparison to WT Ramos B cells (blue). The unstained control (US) is shown in light grey. **C, D.** Flow cytometry analysis of the expression of B cell marker protein on the surface of CD32b KO (beige) or CD32b-tr (orange) in comparison to WT Ramos B cells (blue). The expression data of CD32b KO or CD32b-tr cells are normalized to those of WT Ramos set to 100%. **E.** Fab-PLA study of the IgD-BCR:CD32b proximity on the surface of WT Ramos (upper left), CD32b-tr, (upper right), CD32b KO (lower left), and isolated healthy donor (HD) B cells (lower right). PLA dots in red and the nuclei stained blue by DAPI, Scale bar 5 µm, **F.** Quantification of Fab-PLA data with the CellProfiler and calculation of the significance between the groups with PRISM 10, one-way ANOVA, the Students t-test shows no significant difference between CD32-tr and HD B cells. Mean value are show as red bars.

Figure 3

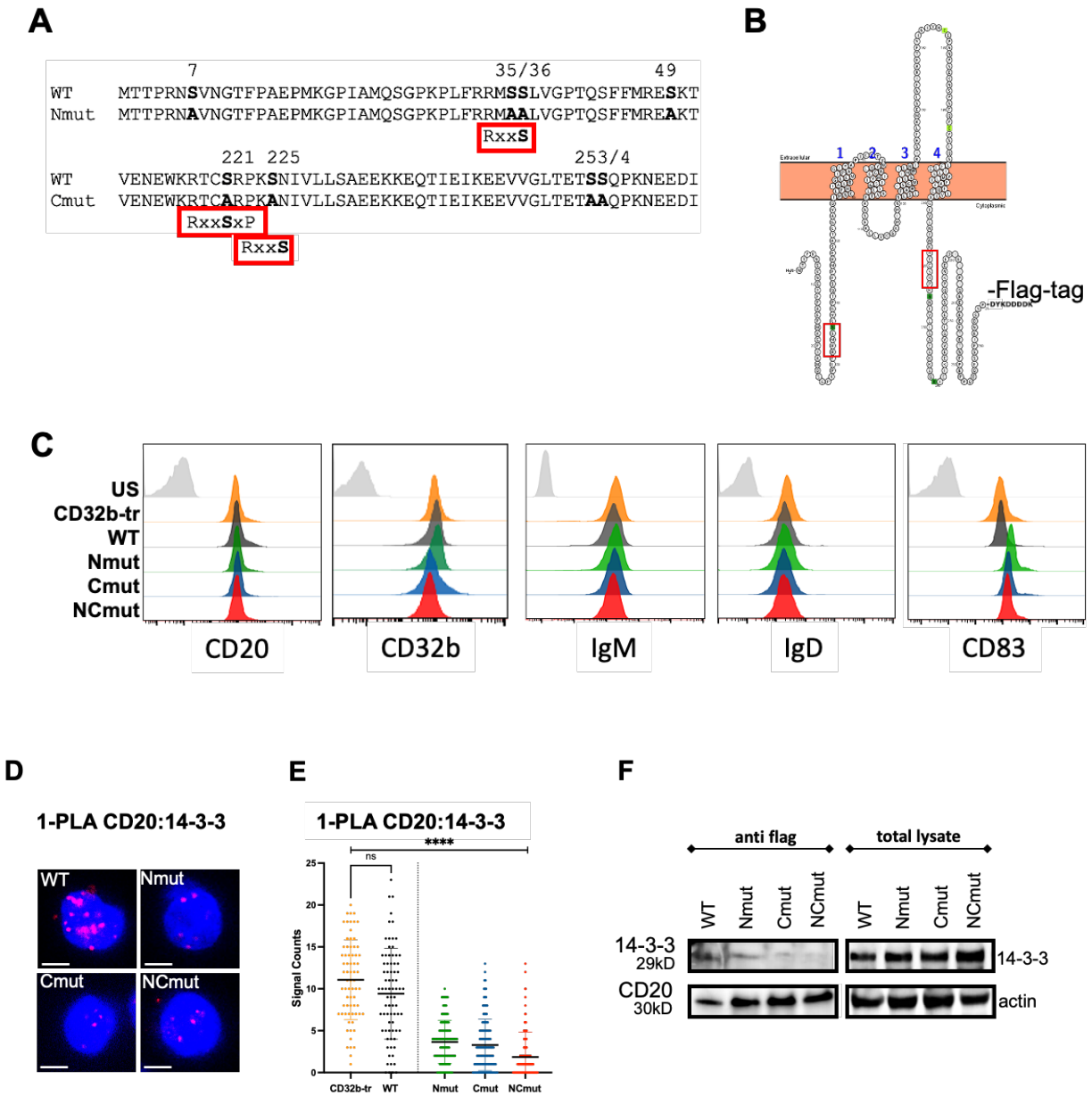

Figure 3:

Mutational analysis of CD20 serine residues and their association with 14-3-3

A. Protein sequence of the N-terminal (top) and part of the C-terminal cytoplasmic tail of human CD20 (bottom). Below the WT sequence the sequence with the introduced S/A mutations (in bold letters) at the N-terminal (Nmut) and C-terminal (Cmut) cytoplasmic tail of CD20 are shown. The location of the RxxS motifs implicated in 14-3-3 binding is shown below the sequence **B.** Membrane topology of human CD20 with a C-terminal flag-tag (CD20-flag). The location of the two RxxS motifs is indicated with red boxes **C**. Flow cytometry analysis of CD32b-tr Ramos cells (orange) and reconstituted Ramos cells expressing CD20 WT (black), Nmut (green), Cmut (dark blue) or NCmut (red). The Ramos cells are tested for the expression of CD20, CD32b, IgM, IgD, and CD83. The unstained (US) CD32-tr cells are shown in grey.

D. Fab-PLA study of the CD20:14-3-3 proximity in WT (upper left), Nmut (upper right), Cmut (lower left), and NCmut (lower right) Ramos B cells. PLA dots in red and the nuclei stained blue by DAPI, Scale bar 5 µm. **E**. Quantification of the PLA data by CellProfiler. Significant differences between groups were calculated with PRISM 10, one-way ANOVA. Students t-test shows no significant difference between CD32-tr and WT Ramos cells. **F.** Western blot analysis of the CD20-flag/14-3-3 association in WT, Nmut, Cmut and NCmut Ramos B cells. The amount of 14-3-3 protein in the anti-flag immunoprecipitated and total lysates is show on the left and right, respectively. Lysates were taken from at least 3 independently generated Ramos cell lines.

Figure 4

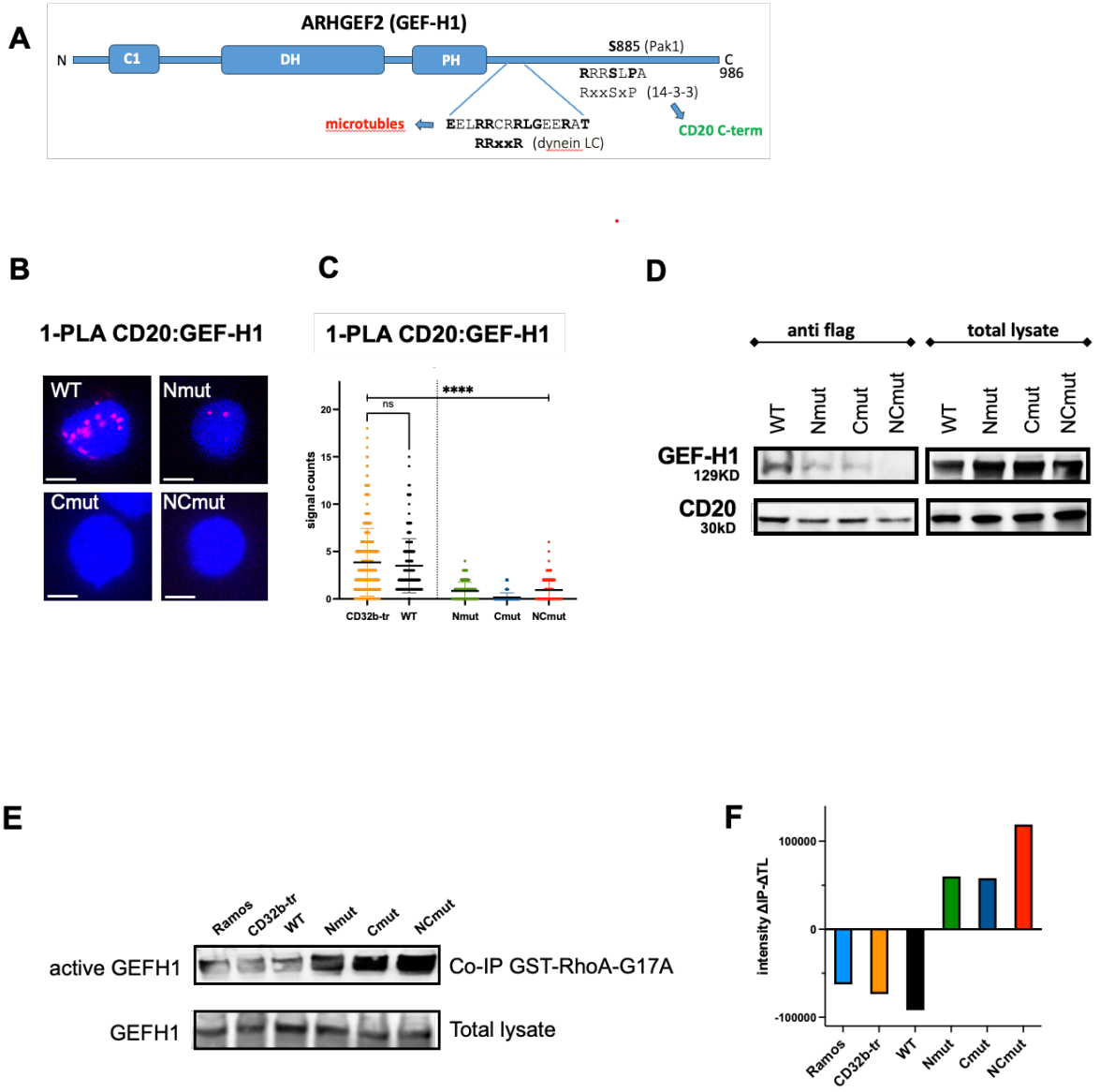

Figure 4:

Constitutive association of CD20 with the GDP/GTP exchange factor GEF-H1.

A. Schematic drawing of the domain structure of the RhoA guanine nucleotide exchange factor GEF-H1 (ARHGEF2). The functional domains are drawn as blue boxes. The location of the RRxxR motif implicated in dynein light chain binding, and the Pak2 phosphorylated S886 within the 14-3-3 binding **R**xx**S**x**P** motif is indicated. **B**. 1-PLA study of the CD20: GEF-H1 proximity in WT (upper left), Nmut (upper right), Cmut (lower left), and NCmut (lower right) Ramos B cells. PLA dots in red and the nuclei stained blue by DAPI, Scale bar 5 µm. **C**. Quantification of PLA of B. with CellProfiler. Significant differences between groups were calculated with PRISM 10, one-way ANOVA. Students t-test shows no significant difference between CD32-tr and WT Ramos cells. **D.** Western blot analysis of the constitutive CD20-flag/GEF-H1 association in WT, Nmut, Cmut and NCmut Ramos B cells. The amount of GEF-H1 protein in the anti-flag immunoprecipitated and total lysates is show on the left and right, respectively. **E.**

Western blot analysis of free GEF-H1 in the lysates of Ramos and CD32b-tr cells as well as reconstituted Ramos cells expressing CD20 WT, Nmut, Cmut or NCmut. The amount of GEF-H1 purified with the GST-RhoAG17A beads and in the total lysate is shown at the top and bottom, respectively. **F.** Quantification of the Western blot data with Image Studio Lite (Licor) showing the difference of signal intensity in the immunoprecipitate (IP) versus that of the total lysates (TL).

Figure 5

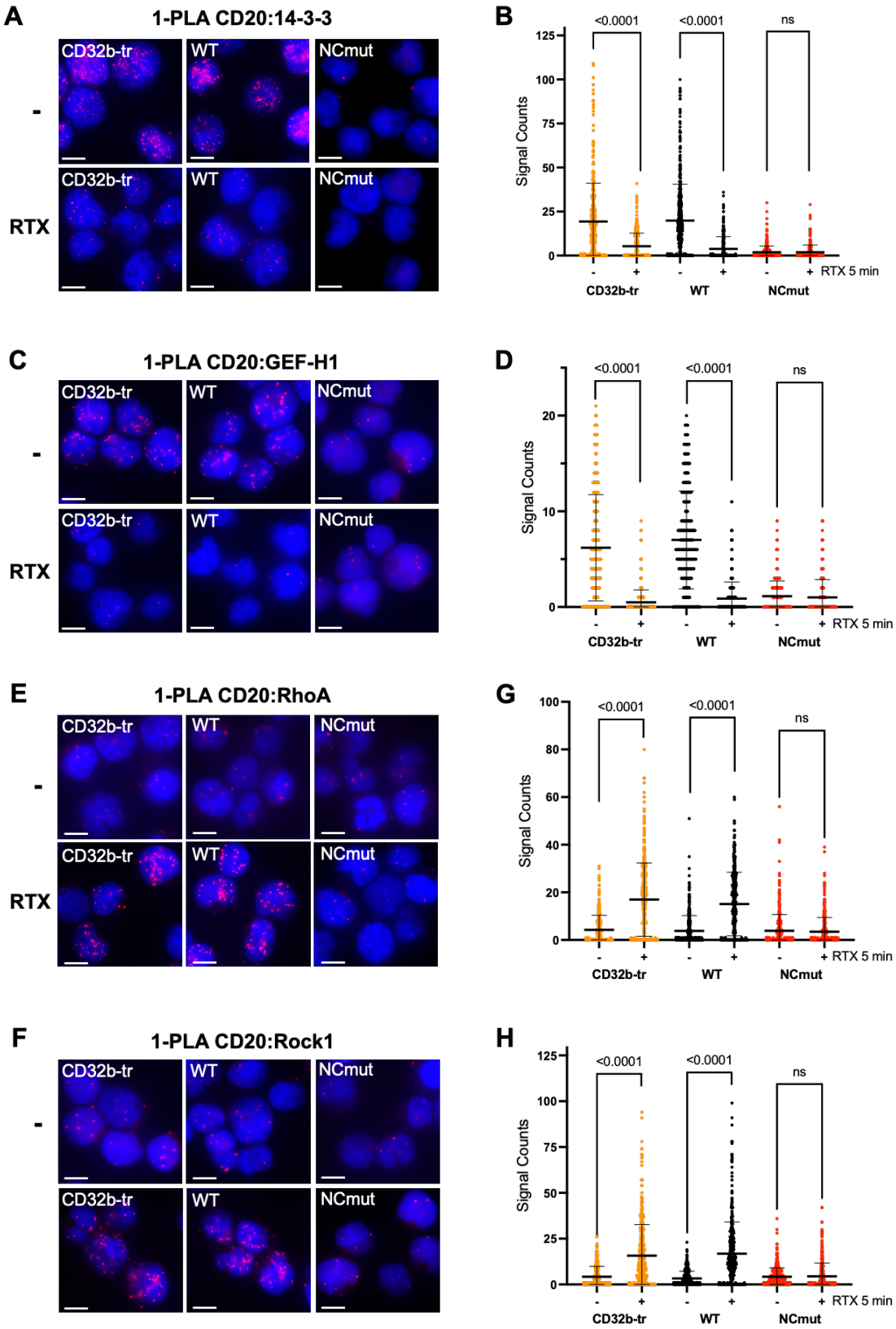

Figure 5:

Loss of GEF-H1 and gain of the RhoA/Rock1 association of CD20 upon RTX treatment

1-PLA study of **A.** the CD20:14-3-3, **C.** the CD20:GEF-H1, **E.** the CD20:RhoA and **F.** the CD20:ROCK1 proximity in CD32b-tr Ramos cells (left) and reconstituted Ramos cells expressing WT (middle) or NCmut CD20 (right). The studied Ramos cells were either untreated (top) or exposed for 5 min to RTX (bottom). PLA dots in red and the nuclei stained blue by DAPI, Scale bar 5 µm. **B**, **D, G, H.** Quantification of the 1-PLA data with CellProfiler. Significant differences between two groups were calculated with PRISM 10 Student's t-test.

Figure 6

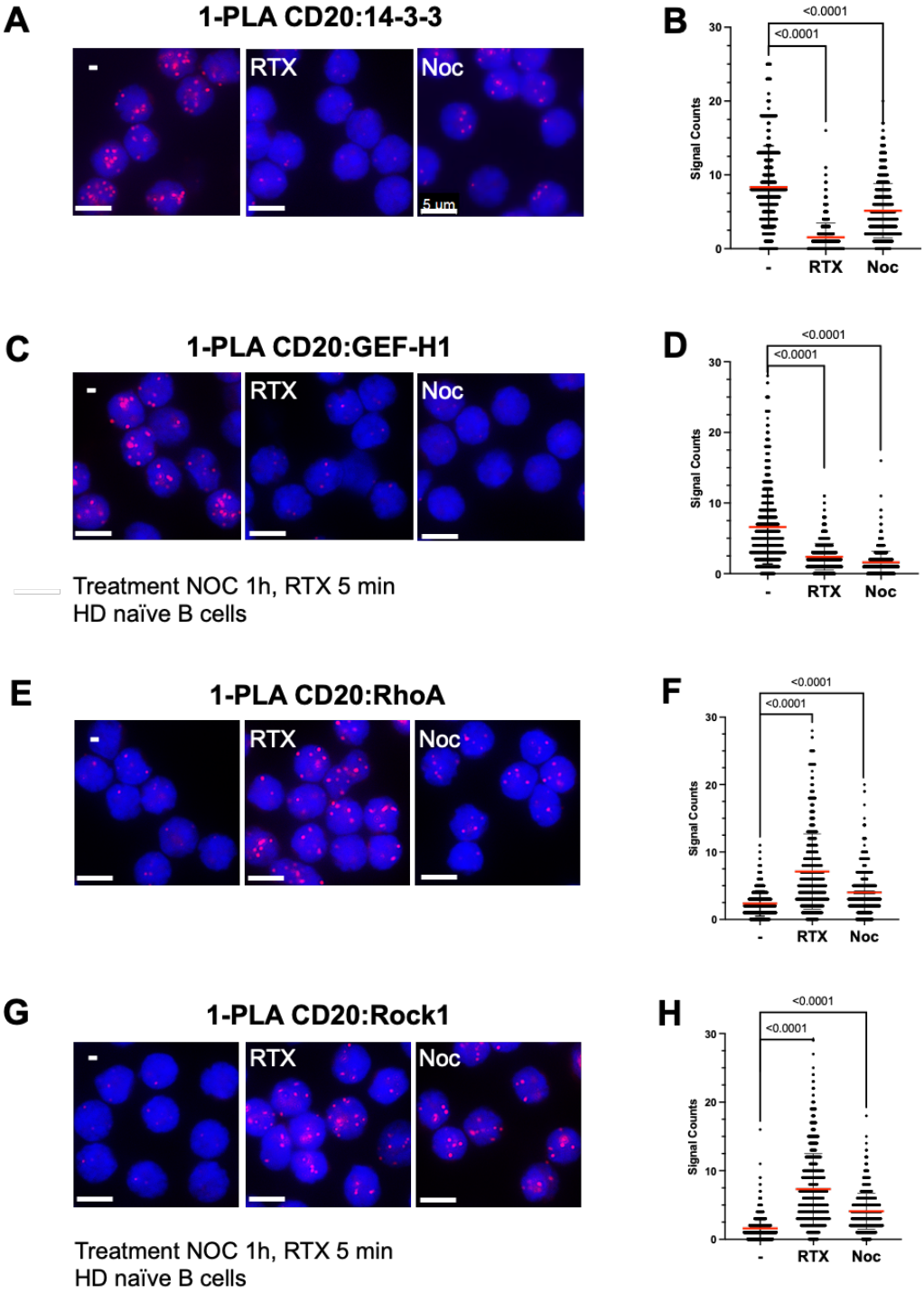

Figure 6:

Altered CD20 association in RTX or nocodazole treated HD B cells

1-PLA study of **A.** the CD20:14-3-3, **C.** the CD20:GEF-H1, **E.** the CD20:RhoA and **F.** the CD20:ROCK1 proximity in unstimulated (left) and HD B cells exposed for 5 min to RTX (middle) or treated for 1 h with Noc (right). PLA dots in red and the nuclei stained blue by DAPI, Scale bar 5 µm. **B**, **D, G, H.** Quantification of the 1-PLA data with CellProfiler. Significant differences between two groups were calculated with PRISM 10 Student's t-test.

Figure 7

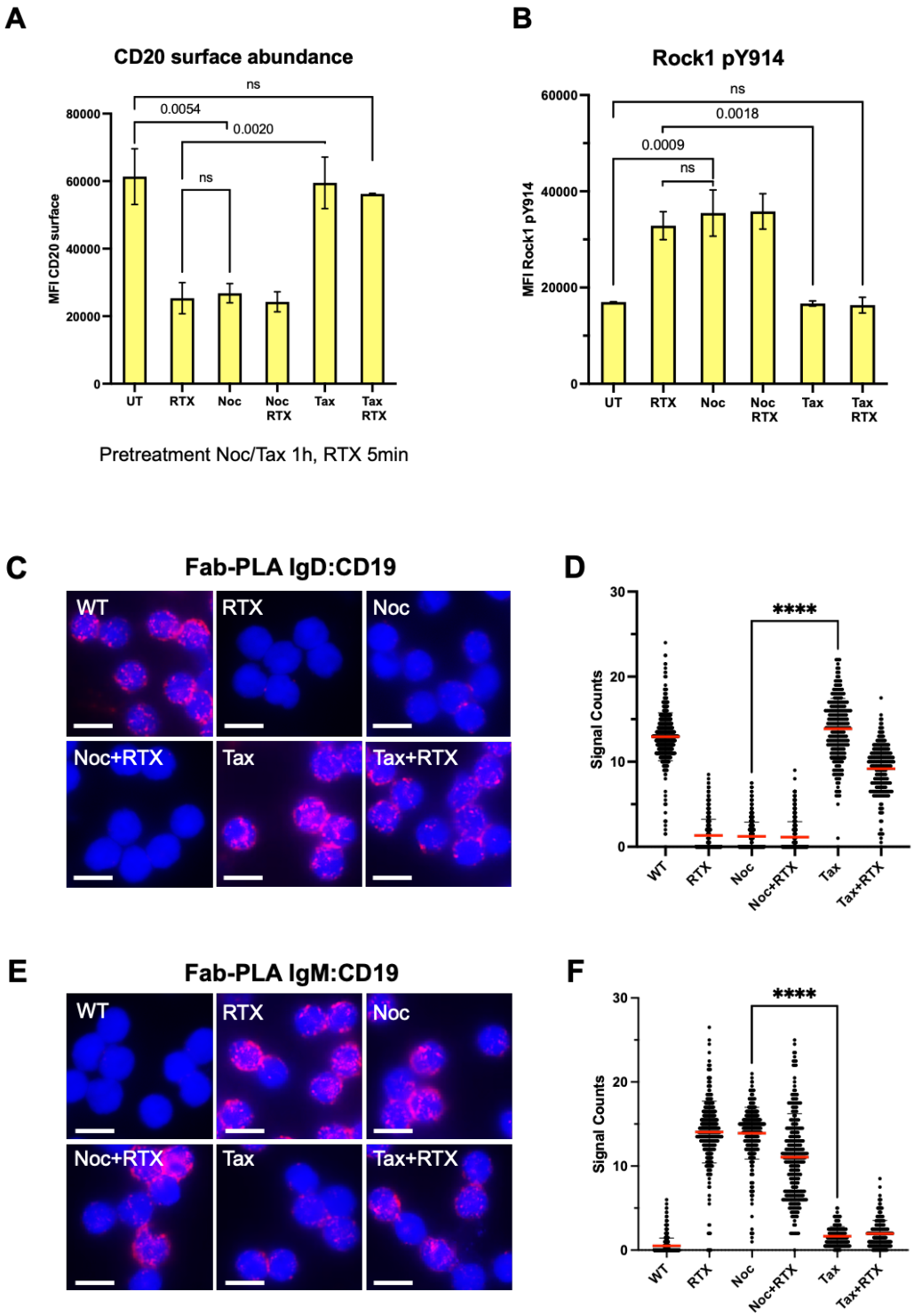

Figure 7:

Stabilization of the IgD-BCR nanocluster and CD20 by the MT network

A. CD20 expression on the surface of untreated (UT) HD B cells or B cells stimulated for 5 min with RTX. As indicated, some of these HD B cells were pretreated for 1 h with either nocodazole (Noc) or docetaxel (Tax). Shown is a summary of the MFI data of >3 flow cytometry experiments. PRISM10 and the students-tests were used to calculated the significant

differences between the experimental groups. **B**. Y914 phosphorylation and activation of Rock1 in untreated (UT) HD B cells or B cells stimulated for 5 min with RTX. As indicated, HD B cells were kept untreated, or pretreated for 1 h with nocodazole (Noc), or docetaxel (Tax). A summary of the MFI data of >3 flow cytometry experiments is presented. Students-tests (Prism10) were used to calculated the significant differences between the groups. Fab-PLA study of **C.** the IgD-BCR:CD19 or **E.** the IgM-BCR:CD19 proximity of HD B cells, kept untreated or stimulated for 5 min with RTX without or with pretreatment of the B cells with either Noc or Tax for 1h as indicated. PLA dots in red and the nuclei stained blue by DAPI, Scale bar 5 µm. **D, F.** Quantification of the Fab-PLA data with CellProfiler. Significant differences between groups were calculated with PRISM 10 Student's t-test.

Figure S1

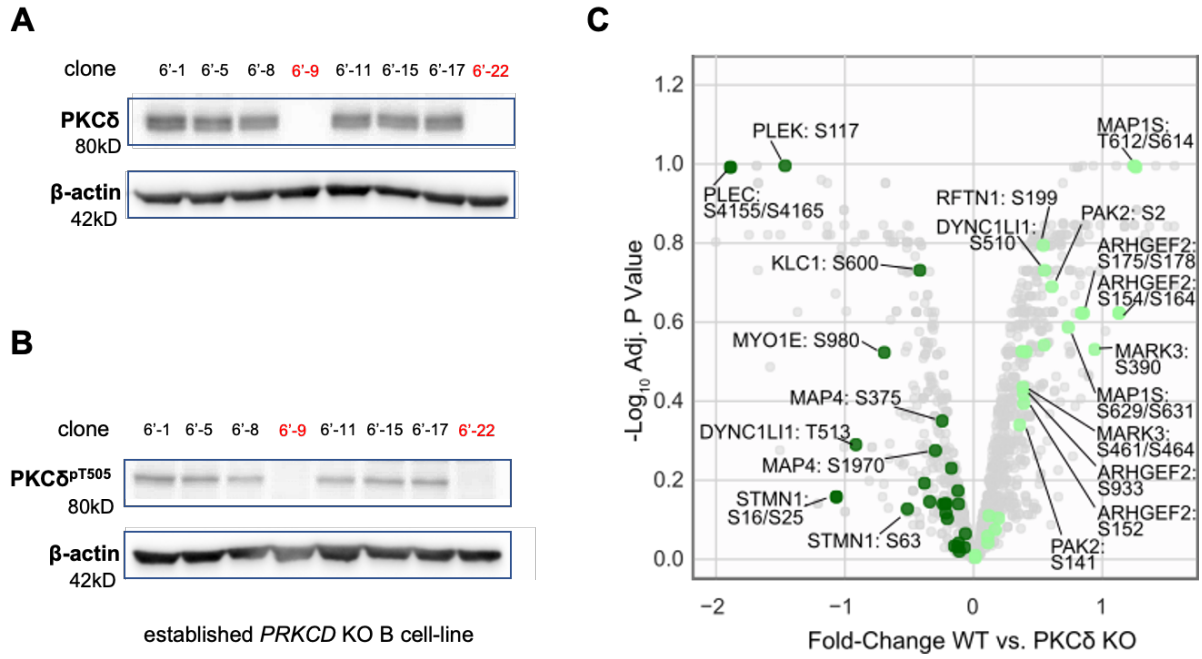

Supplementary figure 1:

Western blot analysis of PKCδ after CRISPR-Cas9 mediated PKCδ KO. Lysates were stained for PKCδ **A**. or PKCδ phospho-threonine 505 (PKCδ pT505) **B**. Clones 6'-9 and 6'-22 were selected for further PKCδ KO studies. **C**. Volcano blot indicating the changes of the constitutive serine or threonine protein phosphosites of PKCδ KO compared to Ramos cells. On the X-axis the plot depicts log2 fold change of phosphorylated serine or threonine residues in the whole proteome of the two cells lines. The Y-axis shows the log10 FDR adjusted p-value. Decreased phosphorylation of serine residues of the MT pathway are shown in dark green, increase in light green. The phosphorylated serine residues of MT proteins are indicated.

Figure S2

A

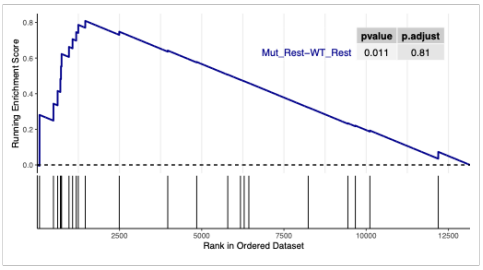

B

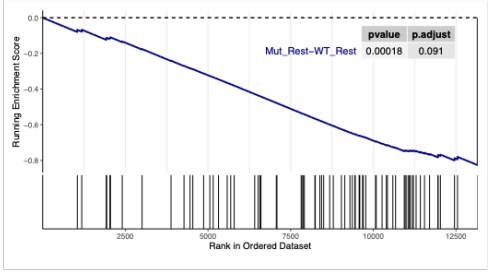

Supplementary figure 2:

Gene set enrichment analysis (GSEA) of genes associated with destabilized MT and cytoskeleton. **A.** The plot shows enrichment of genes associated with positive MT disassembly in PKCδ KO compared to Ramos WT cells. Vertical black lines indicate where genes overexpressed by MT depolymerization fall in the ranked list, (p-value 0.011 and FDR 0.81). **B.** As indication for the disconnection from the actin-cytoskeleton to the plasma membrane the plot shows the decrease of genes essential for the localization of the portion of the cytoskeleton that lies just beneath to the plasma membrane in PKCδ KO compared to Ramos WT cells, (p-value 0.00018 and FDR 0.091). The Normalized Enrichment Score (blue line) considers the ranked list of expression differences between two independent unstimulated PKCδ KO Ramos cell clones and Ramos WT cells.

Figure S3

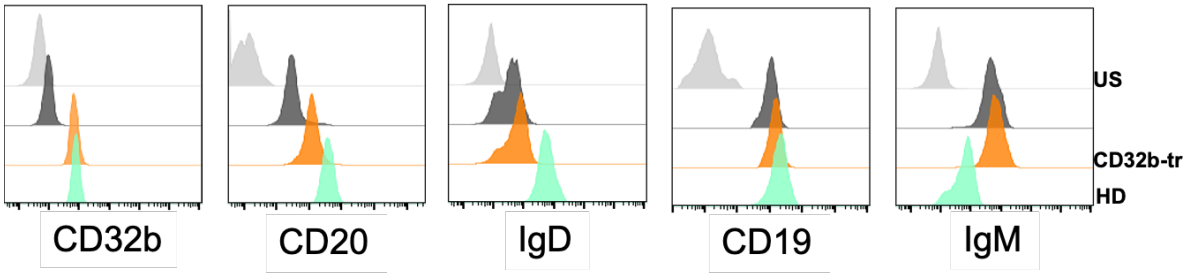

Supplementary figure 3:

Due to the expression of the FcγRIIb receptor on Ramos, the surface abundance of critical B cell proteins more closely resembles that of naive B cells.

Flow cytometry analysis shows the comparison of the expression of B cell surface protein abundance on healthy donor (HD) negative selected naïve B cells (green), Ramos (black) and FcγRIIb receptor transfected (CD32b-tr, orange) Ramos cells. Unstained (US) control in grey).

Figure S4

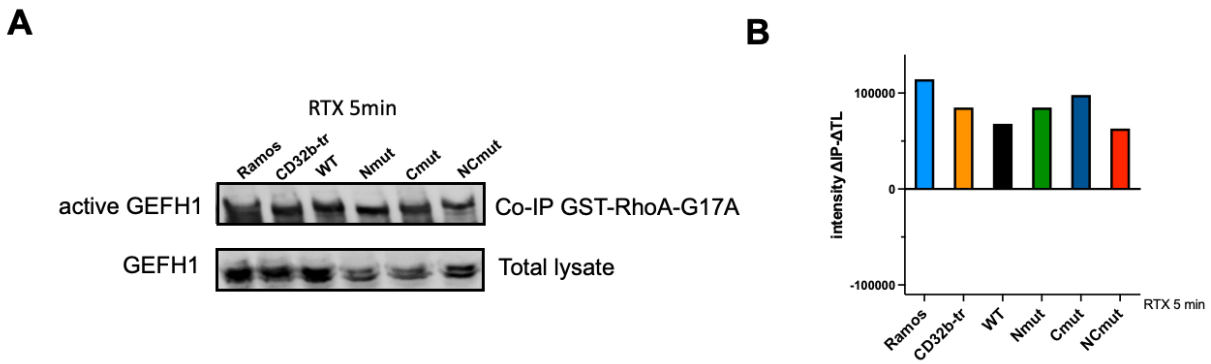

Supplementary figure 4:

Western blot analysis of free GEF-H1 in the lysate of Ramos and CD32b-tr cells as well as reconstituted Ramos cells expressing CD20 WT, Nmut, Cmut or NCmut after activation with RTX for 5 min. The amount of GEF-H1 purified with the GST-RhoAG17A beads and in the total lysate is shown at the top and bottom, respectively. **F.** Quantification of the Western blot data with Image Studio Lite (Licor) showing the difference of signal intensity in the immunoprecipitate (IP) versus that of the total lysates (TL).

Figure S5

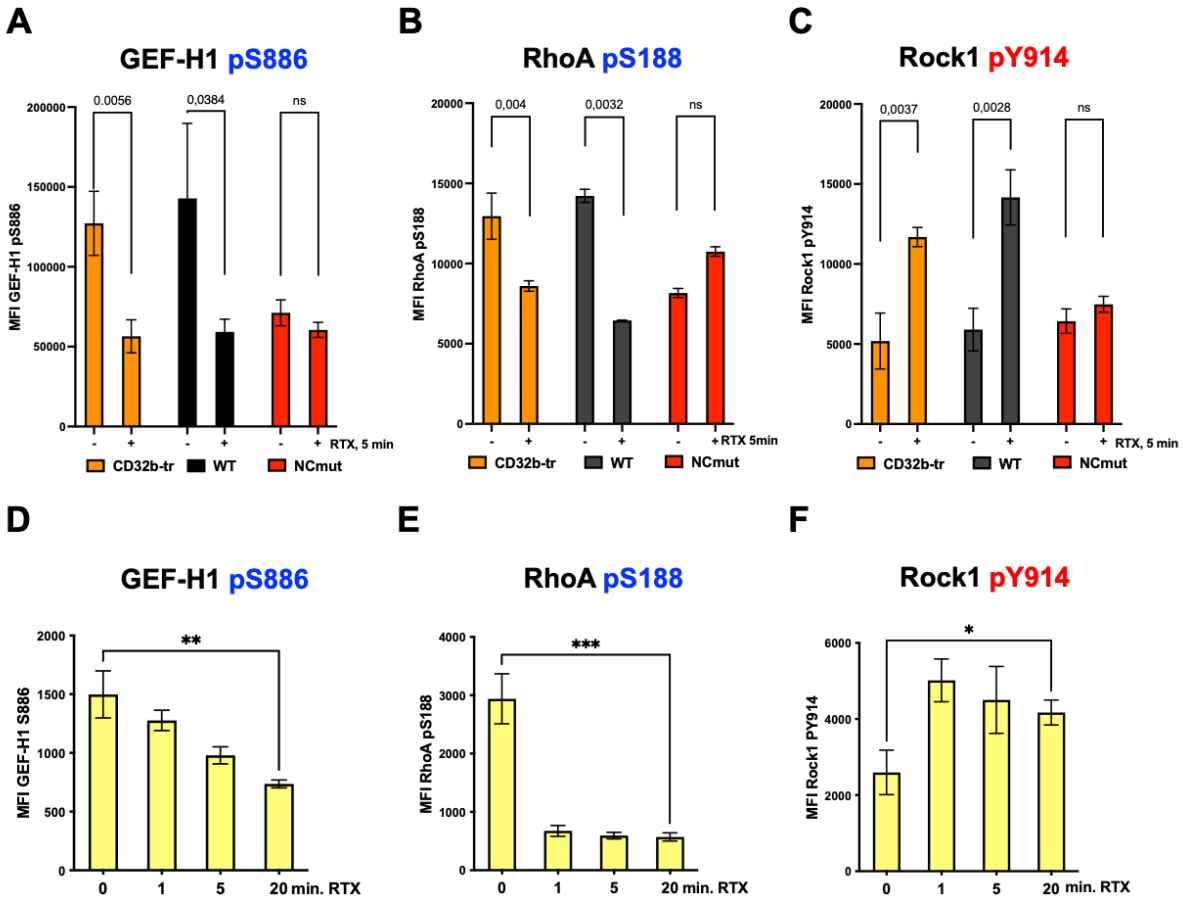

Supplementary figure 5:

Intracellular phospho-flow cytometry analysis of intracellular signal proteins upon RTX treatment for 5 min compared to unstimulated CD20 WT and NCmut S>A transfectant show: **A** Loss of inhibitory GEF-H1 phosphorylation Serine^{886}, which is a prerequisite for the activation of RhoA. **B** Loss of inhibitory RhoA Serine^{188} phosphorylation, which renders RhoA active. RhoA-GTP allows the increase of **C** active Rock1, phosphorylated at Y^{914}**.**

Students t-tests calculated with PRISM 10, show significant differences between the resting and stimulated state of CD32b-tr and WT cells, but not between S>A mutants. Representative NCmut CD20 mutant is presented. **D- F** Intracellular phospho-flow of the same protein residues as in **A-C** but on HD naive B cells and as a time course after RTX stimulation for 0, 1, 5, 20 min. **D** inhibitory GEF-H1 S^{886} phosphorylation, **E** inhibitory RhoA S^{188}, and **F** activatory Rock1 Y914 phosphorylation. Significant differences between the groups were calculated with PRISM 10, one-way ANOVA. Activatory phosphorylations are depicted in red, inhibitory are shown in blue.

Figure S6

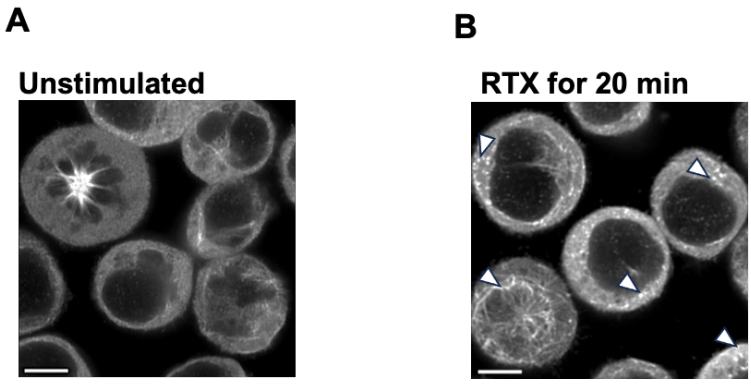

Supplementary figure 6:

Airyscan confocal microscopy images of Ramos CD32b-tr cells **A.** unstimulated or **B.** incubated with RTX for 20 min. Cells were fixed and stained for α-tubulin with Alexa Fluor 555 to visualize MTs. Images present the mid-section of an Airyscan processed z-stack. White arrows in **B.** indicate the peeling of the curved protofilaments away from MT in the treated cells. Scale bar: 5μm.

Figure S7

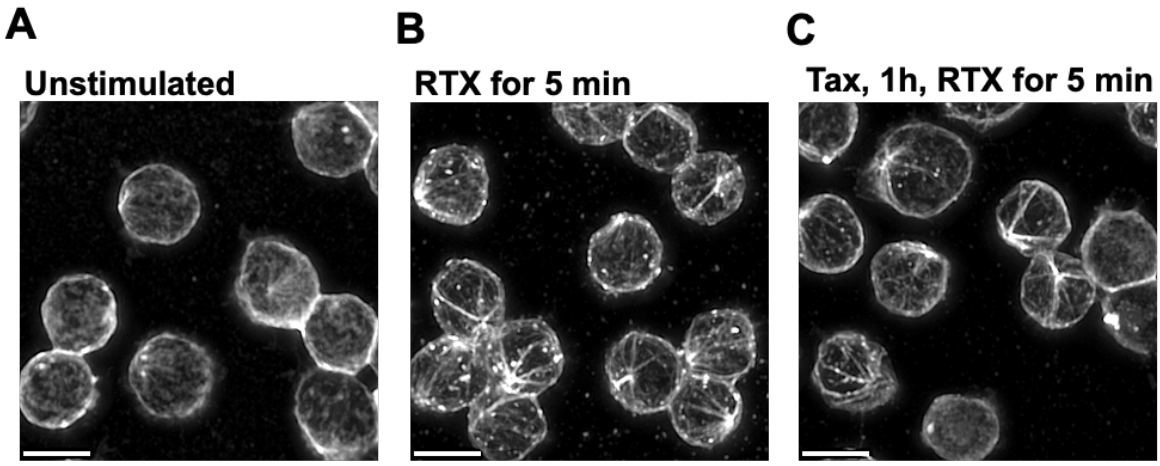

Supplementary figure 7:

Maximum intensity projection of Airyscan (SR) confocal z-stacks of HD naïve B cells **A.** untreated, **B.** upon exposure to RTX for 5 min or **C**. with Taxol pretreatment for 1h before exposure to RTX for 5 min. Cells were fixed and stained for α-tubulin with Alexa Fluor 555. In **B.** background is brightened due to higher presence of dead or destroyed cells. Scale bar: 5μm.

1198 **References:**

1199 1. Getahun A. Role of inhibitory signaling in peripheral B cell tolerance*. *Immunol Rev*.
1200 2022;307(1):27-42. doi:10.1111/imr.13070
1201 2. Kläsener K, Maity PC, Hobeika E, Yang J, Reth M. B cell activation involves
1202 nanoscale receptor reorganizations and inside-out signaling by Syk. *Elife*.
1203 2014;3:e02069. doi:10.7554/eLife.02069
1204 3. Horikawa K, Nishizumi H, Umemori H, Aizawa S, Takatsu K, Yamamoto T.
1205 *Distinctive Roles of Fyn and Lyn in IgD-and IgM-Mediated Signaling*. Vol 11.; 1999.
1206 4. Becker M, Hobeika E, Jumaa H, Reth M, Maity PC. CXCR4 signaling and function
1207 require the expression of the IgD-class B-cell antigen receptor. *Proceedings of the*
1208 *National Academy of Sciences*. Published online May 1, 2017.
1209 doi:10.1073/PNAS.1621512114
1210 5. Geisberger R, Lamers M, Achatz G. The riddle of the dual expression of IgM and IgD.
1211 *Immunology*. 2006;118(4):429-437. doi:10.1111/j.1365-2567.2006.02386.x
1212 6. Maity PC, Blount A, Jumaa H, Ronneberger O, Lillemeier BF, Reth M. B cell antigen
1213 receptors of the IgM and IgD classes are clustered in different protein islands that are
1214 altered during B cell activation. *Sci Signal*. 2015;8(394):ra93.
1215 doi:10.1126/scisignal.2005887
1216 7. Rougé L, Chiang N, Steffek M, et al. Structure of CD20 in complex with the
1217 therapeutic monoclonal antibody rituximab. *Science (1979)*. 2020;367(6483):1224-
1218 1230. doi:10.1126/science.aba3526
1219 8. Deans JP, Li H, Polyak MJ. CD20-mediated apoptosis: signalling through lipid rafts.
1220 *Immunology*. 2002;107(2):176-182. Accessed July 16, 2015.
1221 http://www.pubmedcentral.nih.gov/articlerender.fcgi?artid=1782791&tool=pmcentrez
1222 &rendertype=abstract
1223 9. Reinhardt SCM, Masullo LA, Baudrexel I, et al. Ångström-resolution fluorescence
1224 microscopy. *Nature*. 2023;617(7962):711-716. doi:10.1038/s41586-023-05925-9
1225 10. Pavlasova G, Mraz M. The regulation and function of CD20: An "enigma" of B-cell
1226 biology and targeted therapy. *Haematologica*. 2020;105(6):1494-1506.
1227 doi:10.3324/haematol.2019.243543
1228 11. Riley JK, Sliwkowski MX. CD20: a gene in search of a function. *Semin Oncol*.
1229 2000;27(6 Suppl 12):17-24.
1230 12. Müller M, Gräbnitz F, Barandun N, et al. Light-mediated discovery of surfaceome
1231 nanoscale organization and intercellular receptor interaction networks. *Nat Commun*.
1232 2021;12(1). doi:10.1038/s41467-021-27280-x
1233 13. Arp AB, Abel Gutierrez A, ter Beest M, et al. CD70 recruitment to the immunological
1234 synapse is dependent on CD20 in B cells. *Proceedings of the National Academy of*
1235 *Sciences*. 2025;122(16). doi:10.1073/pnas.2414002122
1236 14. Kosmas C, Stamatopoulos K, Stavroyianni N, Tsavaris N, Papadaki T. Anti-CD20-
1237 based therapy of B cell lymphoma: State of the art. *Leukemia*. 2002;16(10):2004-2015.
1238 doi:10.1038/sj.leu.2402639
1239 15. Smith MR. Rituximab (monoclonal anti-CD20 antibody): Mechanisms of action and
1240 resistance. *Oncogene*. 2003;22(47):7359-7368. doi:10.1038/sj.onc.1206939
1241 16. Margoni M, Preziosa P, Filippi M, Rocca MA. Anti-CD20 therapies for multiple
1242 sclerosis: current status and future perspectives. *J Neurol*. 2022;269(3):1316-1334.
1243 doi:10.1007/s00415-021-10744-x
1244 17. Jazirehi AR, Bonavida B. Cellular and molecular signal transduction pathways
1245 modulated by rituximab (rituxan, anti-CD20 mAb) in non-Hodgkin's lymphoma:
1246 Implications in chemosensitization and therapeutic intervention. *Oncogene*.
1247 2005;24(13):2121-2143. doi:10.1038/sj.onc.1208349
1248 18. Klein C, Jamois C, Nielsen T. Anti-CD20 treatment for B-cell malignancies: current
1249 status and future directions. *Expert Opin Biol Ther*. 2021;21(2):161-181.
1250 doi:10.1080/14712598.2020.1822318

1251 19. Payandeh Z, Bahrami AA, Hoseinpoor R, et al. The applications of anti-CD20
1252 antibodies to treat various B cells disorders. *Biomedicine and Pharmacotherapy*.
1253 2019;109:2415-2426. doi:10.1016/j.biopha.2018.11.121
1254 20. Boross P, Leusen JHW. Mechanisms of action of CD20 antibodies. *Am J Cancer Res*.
1255 2012;2(6):676-690.
1256 21. Kläsener K, Jellusova J, Andrieux G, et al. CD20 as a gatekeeper of the resting state of
1257 human B cells. *Proc Natl Acad Sci U S A*. 2021;118(7). doi:10.1073/pnas.2021342118
1258 22. Salzer E, Santos-Valente E, Keller B, Warnatz K, Boztug K. Protein Kinase C δ: a
1259 Gatekeeper of Immune Homeostasis. *J Clin Immunol*. 2016;36(7):631-640.
1260 doi:10.1007/s10875-016-0323-0
1261 23. Lim PS, Sutton CR, Rao S. Protein kinase C in the immune system: From signalling to
1262 chromatin regulation. *Immunology*. 2015;146(4):508-522. doi:10.1111/imm.12510
1263 24. Pracht C, Minguet S, Leitges M, Reth M, Huber M. Association of protein kinase C-δ
1264 with the B cell antigen receptor complex. *Cell Signal*. 2007;19(4):715-722.
1265 doi:10.1016/j.cellsig.2006.07.023
1266 25. Sjef Verbeek J, Hirose S, Nishimura H. The complex association of fcγriib with
1267 autoimmune susceptibility. *Front Immunol*. 2019;10(OCT).
1268 doi:10.3389/fimmu.2019.02061
1269 26. Karnell JL, Dimasi N, Karnell FG, et al. CD19 and CD32b Differentially Regulate
1270 Human B Cell Responsiveness. *The Journal of Immunology*. 2014;192(4):1480-1490.
1271 doi:10.4049/jimmunol.1301361
1272 27. McCaleb MR, Miranda AM, Ratliff KC, Torres RM, Pelanda R. CD19 Is Internalized
1273 Together with IgM in Proportion to B Cell Receptor Stimulation and Is Modulated by
1274 Phosphatidylinositol 3-Kinase in Bone Marrow Immature B Cells. *Immunohorizons*.
1275 2023;7(1):49-63. doi:10.4049/immunohorizons.2200092
1276 28. Kläsener K, Yang J, Reth M. *Study B Cell Antigen Receptor Nano-Scale Organization*
1277 *by in Situ Fab Proximity Ligation Assay*. Vol 1707.; 2018. doi:10.1007/978-1-4939-
1278 7474-0_12
1279 29. Tinti M, Johnson C, Toth R, Ferrier DEK, Mackintosh C. Evolution of signal
1280 multiplexing by 14-3-3-binding 2R-ohnologue protein families in the vertebrates. *Open*
1281 *Biol*. 2012;2(7):120103. doi:10.1098/rsob.120103
1282 30. Pitasse-Santos P, Hewitt-Richards I, Abeywickrama Wijewardana Sooriyaarachchi
1283 MD, Doveston RG. Harnessing the 14-3-3 protein–protein interaction network. *Curr*
1284 *Opin Struct Biol*. 2024;86. doi:10.1016/j.sbi.2024.102822
1285 31. Omasits U, Ahrens CH, Müller S, Wollscheid B. Protter: interactive protein feature
1286 visualization and integration with experimental proteomic data. *Bioinformatics*.
1287 2014;30(6):884-886. doi:10.1093/bioinformatics/btt607
1288 32. Ivaldi C, Martin BR, Kieffer-Jaquinod S, et al. Proteomic analysis of S-Acylated
1289 proteins in human B cells reveals palmitoylation of the immune regulators CD20 and
1290 CD23. *PLoS One*. 2012;7(5). doi:10.1371/journal.pone.0037187
1291 33. Li Z, Ju X, Silveira PA, Abadir E, Hsu W hsun. CD83 : Activation Marker for Antigen
1292 Presenting Cells and Its Therapeutic Potential. 2019;10(June):1-9.
1293 doi:10.3389/fimmu.2019.01312
1294 34. Ren Y, Li R, Zheng Y, Busch H. *Cloning and Characterization of GEF-H1, a*
1295 *Microtubule-Associated Guanine Nucleotide Exchange Factor for Rac and Rho*
1296 *GTPases**. Vol 273.; 1998. http://www.jbc.org
1297 35. Zenke FT, Krendel M, DerMardirossian C, King CC, Bohl BP, Bokoch GM. p21-
1298 activated Kinase 1 Phosphorylates and Regulates 14-3-3 Binding to GEF-H1, a
1299 Microtubule-localized Rho Exchange Factor. *Journal of Biological Chemistry*.
1300 2004;279(18):18392-18400. doi:10.1074/jbc.M400084200
1301 36. Krendel M, Zenke FT, Bokoch GM. Nucleotide exchange factor GEF-H1 mediates
1302 cross-talk between microtubules and the actin cytoskeleton. *Nat Cell Biol*.
1303 2002;4(4):294-301. doi:10.1038/ncb773

1304 37. Meiri D, Marshall CB, Mokady D, et al. Mechanistic insight into GPCR-mediated
1305 activation of the microtubule-associated RhoA exchange factor GEF-H1. *Nat Commun*.
1306 2014;5. doi:10.1038/ncomms5857
1307 38. Kashyap AS, Fernandez-Rodriguez L, Zhao Y, et al. GEF-H1 Signaling upon
1308 Microtubule Destabilization Is Required for Dendritic Cell Activation and Specific
1309 Anti-tumor Responses. *Cell Rep*. 2019;28(13):3367-3380.e8.
1310 doi:10.1016/j.celrep.2019.08.057
1311 39. Kopf A, Kiermaier E. Dynamic Microtubule Arrays in Leukocytes and Their Role in
1312 Cell Migration and Immune Synapse Formation. *Front Cell Dev Biol*. 2021;9.
1313 doi:10.3389/fcell.2021.635511
1314 40. Kosoff R, Chows HY, Radus M, Chernoffs J. Pak2 kinase restrains mast cell FcεRI
1315 receptor signaling through modulation of rho protein guanine nucleotide exchange
1316 factor (GEF) activity. *Journal of Biological Chemistry*. 2013;288(2):974-983.
1317 doi:10.1074/jbc.M112.422295
1318 41. Waheed F, Speight P, Dan Q, Garcia-Mata R, Szaszi K. Affinity precipitation of active
1319 Rho-GEFs using a GST-tagged mutant Rho protein (GST-RhoA(G17A)) from
1320 epithelial cell lysates. *J Vis Exp*. 2012;(61). doi:10.3791/3932
1321 42. Sluchanko NN, Gusev NB. 14-3-3 Proteins and regulation of cytoskeleton.
1322 *Biochemistry (Moscow)*. 2010;75(13):1528-1546. doi:10.1134/S0006297910130031
1323 43. Brandwein D, Wang Z. Interaction between Rho GTPases and 14-3-3 proteins. *Int J*
1324 *Mol Sci*. 2017;18(10). doi:10.3390/ijms18102148
1325 44. Julian L. *Investigating the Role of Caspase Cleavage of ROCK1 in Tissue Homeostasis*
1326 *and Tumour Development*.; 2015.
1327 45. Olson MF. Rho-associated coiled-coil containing kinases (ROCK): structure,
1328 regulation, and functions. *Small GTPases*. 2014;5:e29846. doi:10.4161/sgtp.29846
1329 46. Birkenfeld J, Nalbant P, Yoon SH, Bokoch GM. Cellular functions of GEF-H1, a
1330 microtubule-regulated Rho-GEF: is altered GEF-H1 activity a crucial determinant of
1331 disease pathogenesis? *Trends Cell Biol*. 2008;18(5):210-219.
1332 doi:10.1016/j.tcb.2008.02.006
1333 47. Pineau J, Pinon L, Mesdjian O, Fattaccioli J, Duménil AML, Pierobon P. Microtubules
1334 restrict F-actin polymerization to the immune synapse via GEF-H1 to maintain polarity
1335 in lymphocytes. Published online January 3, 2022. doi:10.1101/2022.01.03.473915
1336 48. Mandelkow EM, Mandelkow E, Milligan RA. *Microtubule Dynamics and Microtubule*
1337 *Caps: A Time-Resolved Cryo-Electron Microscopy Study*.
1338 49. Downing KH, Nogales E. Cryoelectron Microscopy Applications in the Study of
1339 Tubulin Structure, Microtubule Architecture, Dynamics and Assemblies, and
1340 Interaction of Microtubules with Motors. In: *Methods in Enzymology*. Vol 483.
1341 Academic Press Inc.; 2010:121-142. doi:10.1016/S0076-6879(10)83006-X
1342 50. Basu A, Worth F, States U. Two Faces of Protein Kinase C δ : The Contrasting Roles
1343 of PKC δ in Cell Survival and Cell Death. 2015;(August). doi:10.1100/tsw.2010.214
1344 51. Gada KD, Logothetis DE. PKC regulation of ion channels: The involvement of PIP2.
1345 *Journal of Biological Chemistry*. 2022;298(6). doi:10.1016/j.jbc.2022.102035
1346 52. Miyamoto. Increased proliferation of B cells and auto-immunity in mice lacking
1347 protein kinase Cd. *Nature*. 2002;(volume 416):865.
1348 53. Sun Kuehn H, Niemela JE, Rangel-Santos A, et al. Loss-of-function of the protein
1349 kinase C d (PKCd) causes a B-cell lymphoproliferative syndrome in humans. *Blood*.
1350 2013;121(16):3117-3125. doi:10.1182/blood
1351 54. Merino-Cortés S V, Gardeta SR, Roman-Garcia S, et al. *Diacylglycerol Kinase ζ*
1352 *Promotes Actin Cytoskeleton Remodeling and Mechanical Forces at the B Cell*
1353 *Immune Synapse*. Vol 13.; 2020. https://www.science.org
1354 55. Chari R, Kim S, Murugappan S, Sanjay A, Daniel JL, Kunapuli SP. Lyn, PKC-δ,
1355 SHIP-1 interactions regulate GPVI-mediated platelet-dense granule secretion. *Blood*.
1356 2009;114(14):3056-3063. doi:10.1182/blood-2008-11-188516

56. Kajimoto T, Sawamura S, Tohyama Y, Mori Y, Newton AC. Protein kinase C δ-specific activity reporter reveals agonist-evoked nuclear activity controlled by Src family of kinases. *Journal of Biological Chemistry*. 2010;285(53):41896-41910. doi:10.1074/jbc.M110.184028
57. Johnson C, Crowther S, Stafford MJ, Campbell DG, Toth R, MacKintosh C. Bioinformatic and experimental survey of 14-3-3-binding sites. *Biochemical Journal*. 2010;427(1):69-78. doi:10.1042/BJ20091834
58. Pennington K, Chan T, Torres M, Andersen J. The dynamic and stress-adaptive signaling hub of 14-3-3: emerging mechanisms of regulation and context-dependent protein–protein interactions. *Oncogene*. 2018;37(42):5587-5604. doi:10.1038/s41388-018-0348-3
59. Paul AL, Denison FC, Schultz ER, Zupanska AK, Ferl RJ. 14-3-3 Phosphoprotein interaction networks - Does isoform diversity present functional interaction specification? *Front Plant Sci*. 2012;3(AUG). doi:10.3389/fpls.2012.00190
60. Joo E, Olson MF. Regulation and functions of the RhoA regulatory guanine nucleotide exchange factor GEF-H1. *Small GTPases*. 2021;12(5-6):358-371. doi:10.1080/21541248.2020.1840889
61. Azoitei ML, Noh J, Marston DJ, et al. Spatiotemporal dynamics of GEF-H1 activation controlled by microtubule- And Src-mediated pathways. *Journal of Cell Biology*. 2019;218(9):3077-3097. doi:10.1083/JCB.201812073
62. Mok YK, Lo KWH, Zhang M. Structure of Tctex-1 and Its Interaction with Cytoplasmic Dynein Intermediate Chain. *Journal of Biological Chemistry*. 2001;276(17):14067-14074. doi:10.1074/jbc.M011358200
63. Meiri D, Marshall CB, Greeve MA, et al. Mechanistic Insight into the Microtubule and Actin Cytoskeleton Coupling through Dynein-Dependent RhoGEF Inhibition. *Mol Cell*. 2012;45(5):642-655. doi:10.1016/j.molcel.2012.01.027
64. van de Ven AAJM, Compeer EB, Bloem AC, et al. Defective calcium signaling and disrupted CD20-B-cell receptor dissociation in patients with common variable immunodeficiency disorders. *J Allergy Clin Immunol*. 2012;129(3):755-761.e7. doi:10.1016/j.jaci.2011.10.020
65. Li H, Ayer LM, Polyak MJ, et al. The CD20 calcium channel is localized to microvilli and constitutively associated with membrane rafts: Antibody binding increases the affinity of the association through an epitope-dependent cross-linking-independent mechanism. *Journal of Biological Chemistry*. 2004;279(19):19893-19901. doi:10.1074/jbc.M400525200
66. Schober R, Waldherr L, Schmidt T, et al. STIM1 and Orai1 regulate Ca 2+ microdomains for activation of transcription. *Biochim Biophys Acta Mol Cell Res*. 2019;1866(7):1079-1091. doi:10.1016/j.bbamcr.2018.11.001
67. Fais S, Malorni W. Leukocyte uropod formation and membrane/cytoskeleton linkage in immune interactions. *J Leukoc Biol*. 2003;73(5):556-563. doi:10.1189/jlb.1102568
68. Saltukoglu D, Özdemir B, Holtmannspötter M, et al. Plasma membrane topography governs the 3D dynamic localization of IgM B cell antigen receptor clusters. *EMBO J*. 2023;42(4):e112030. doi:10.15252/embj.2022112030
69. Mattila PK, Batista FD, Treanor B. Dynamics of the actin cytoskeleton mediates receptor cross talk: An emerging concept in tuning receptor signaling. *J Cell Biol*. 2016;212(3).
70. Wang J, Lin F, Wan Z, et al. *I M M U N O L O G Y Profiling the Origin, Dynamics, and Function of Traction Force in B Cell Activation*.; 2018. https://www.science.org
71. Sanchez-Madrid F. SJ. Bringing up the rear- defining the roles of the uropod. *Nat Rev Mol Cell Biol*. 2009;Volume 10:353-359.
72. Roberts PJ, Mitin N, Keller PJ, et al. Rho family GTPase modification and dependence on CAAX motif-signaled posttranslational modification. *Journal of Biological Chemistry*. 2008;283(37):25150-25163. doi:10.1074/jbc.M800882200

1410 73. Lehtimäki JI, Rajakylä EK, Tojkander S, Lappalainen P. Generation of stress fibers
1411 through myosin-driven reorganization of the actin cortex. *Elife*. 2021;10:1-43.
1412 doi:10.7554/eLife.60710
1413 74. Rey M, Sanchez-Madrid F, Valenzuela-Fernandez A. *The Role of Actomyosin and the*
1414 *Microtubular Network in Both the Immunological Synapse and T Cell Activation*. Vol
1415 12.; 2007.
1416 75. Reth M. Discovering immunoreceptor coupling and organization motifs. *Front*
1417 *Immunol*. 2023;14. doi:10.3389/fimmu.2023.1253412
1418 76. Shanehbandi D, Majidi J, Kazemi T, Baradaran B, Aghebati-Maleki L. CD20-based
1419 Immunotherapy of B-cell Derived Hematologic Malignancies. *Curr Cancer Drug*
1420 *Targets*. 2017;17(5):423-444. doi:10.2174/1568009617666170109151128
1421 77. Deans JP, Li H, Polyak MJ. *CD20-Mediated Apoptosis: Signalling through Lipid*
1422 *Rafts*.; 2002.
1423 78. Chang YC, Nalbant P, Birkenfeld J, Chang ZF, Bokoch GM. 3GEF-H1 couples
1424 nocodazole-induced microtubule disassembly to cell contractility via RhoA. *Mol Biol*
1425 *Cell*. 2008;19(5):2147-2153. doi:10.1091/mbc.E07-12-1269
1426 79. Kozlova V, Ledererova A, Ladungova A, et al. CD20 is dispensable for B-cell receptor
1427 signaling but is required for proper actin polymerization, adhesion and migration of
1428 malignant B cells. *PLoS One*. 2020;15(3). doi:10.1371/journal.pone.0229170
1429 80. Hiraga J, Tomita A, Sugimoto T, et al. Down-regulation of CD20 expression in B-cell
1430 lymphoma cells after treatment with rituximab-containing combination
1431 chemotherapies: its prevalence and clinical significance. Published online 2009.
1432 doi:10.1182/blood-2008-08
1433 81. Marshalek JP, Dragan M, Tomassetti S, Labarbera K, Amaya A, Har ; *E19537*
1434 *Publication Only CD20 and CD19 Expression Loss in Relapsed or Refractory B-Cell*
1435 *Non-Hodgkin Lymphoma: A Retrospective Cohort*.; 2022.
1436 82. Däbritz JHM, Yu Y, Milanovic M, et al. CD20-targeting immunotherapy promotes
1437 cellular senescence in B-cell lymphoma. *Mol Cancer Ther*. 2016;15(5):1074-1081.
1438 doi:10.1158/1535-7163.MCT-15-0627
1439 83. Chen Y, Chen L, Lun ATL, Baldoni PL, Smyth GK. edgeR v4: powerful differential
1440 analysis of sequencing data with expanded functionality and improved support for
1441 small counts and larger datasets. *Nucleic Acids Res*. 2025;53(2).
1442 doi:10.1093/nar/gkaf018
1443 84. Wu T, Hu E, Xu S, et al. clusterProfiler 4.0: A universal enrichment tool for
1444 interpreting omics data. *Innovation*. 2021;2(3). doi:10.1016/j.xinn.2021.100141
1445 85. Subramanian A, Tamayo P, Mootha VK, et al. *Gene Set Enrichment Analysis: A*
1446 *Knowledge-Based Approach for Interpreting Genome-Wide Expression Profiles*.; 2005.
1447 www.pnas.orgcgidoi10.1073pnas.0506580102
1448 86. Wang JC, Bolger-Munro M, Gold MR. Visualizing the actin and microtubule
1449 cytoskeletons at the b-cell immune synapse using stimulated emission depletion
1450 (STED) microscopy. *Journal of Visualized Experiments*. 2018;2018(134).
1451 doi:10.3791/57028
1452 87. Cox J, Mann M. MaxQuant enables high peptide identification rates, individualized
1453 p.p.b.-range mass accuracies and proteome-wide protein quantification. *Nat*
1454 *Biotechnol*. 2008;26(12):1367-1372. doi:10.1038/nbt.1511
1455 88. Cox J, Neuhauser N, Michalski A, Scheltema RA, Olsen J V., Mann M. Andromeda: A
1456 peptide search engine integrated into the MaxQuant environment. *J Proteome Res*.
1457 2011;10(4):1794-1805. doi:10.1021/pr101065j
1458 89. Bender J, Mühlhäuser WWD, Zimmerman JP, Drepper F, Warscheid B. Autoprot:
1459 Processing, Analysis and Visualization of Proteomics Data in Python. Published online
1460 January 23, 2024. doi:10.1101/2024.01.18.571429
1461